Title: Largest recent impact craters on Mars: Orbital imaging and surface seismic co-investigation

Authors: L. V. Posiolova[1]*, P. Lognonné[2], W. B. Banerdt[3], J. Clinton[4], G. S. Collins[5], T. Kawamura[2], S. Ceylan[6], I. Daubar[7], B. Fernando[8], M. Froment[2,9], D. Giardini[6], M. C. Malin[1], K. Miljković[10], S. C. Stähler[6], Z. Xu[2], M. E. Banks[11], É. Beucler[12], B. A. Cantor[1], C. Charalambous[13], N. Dahmen[6], P. Davis[14], M. Drilleau[15], C. M. Dundas[16], C. Durán[6], F. Euchner[6], R. F. Garcia[15], M. Golombek[3], A. Horleston[17], C. Keegan[1], A. Khan[6,18], D. Kim[6], C. Larmat[9], R. Lorenz[19], L. Margerin[20], S. Menina[2], M. Panning[3], C. Pardo[2], C. Perrin[12], W. T. Pike[13], M. Plasman[2], A. Rajšić[10]†, L. Rolland[21], E. Rougier[9], G. Speth[1], A. Spiga[22], A. Stott[15], D. Susko[1], N. A. Teanby[17], A. Valeh[1], A. Werynski[1], N. Wójcicka[5], G. Zenhäusern[6].

Affiliations:

[1]Malin Space Science Systems, San Diego, CA, USA.
[2]Université Paris Cité, Institut de Physique du Globe de Paris, CNRS, Paris, France.
[3]Jet Propulsion Laboratory, California Institute of Technology, Pasadena, CA, USA.
[4]Swiss Seismological Service, ETH Zurich, Zurich, Switzerland.
[5]Department of Earth Science and Engineering, Imperial College London, London, UK.
[6]Institute of Geophysics, ETH Zurich, Zurich, Switzerland.
[7]Department of Earth, Environmental, and Planetary Sciences, Brown University, Providence, RI, USA.
[8]Department of Earth Sciences, University of Oxford, Oxford, UK.
[9]Earth and Environmental Sciences Division, Los Alamos National Laboratory, Los Alamos, NM, USA.
[10]Space Science and Technology Centre, School of Earth and Planetary Sciences, Curtin University, Perth, Australia.
[11]NASA Goddard Space Flight Center, Greenbelt, MD, USA.
[12]Laboratoire de Planétologie et Géodynamique, UMR6112, Université de Nantes, Université d'Angers, CNRS, Nantes, France.
[13]Department of Electrical and Electronic Engineering, Imperial College London, London, UK.
[14]Department of Earth, Planetary and Space Sciences, University of California, Los Angeles, CA, USA.
[15]Institut Supérieur de l'Aéronautique et de l'Espace SUPAERO, Toulouse, France.
[16]U. S. Geological Survey, Astrogeology Science Center, Flagstaff, AZ, USA.
[17]School of Earth Sciences, University of Bristol, Bristol, UK.
[18]Physik-Institut, University of Zurich, Zurich, Switzerland.
[19]Johns Hopkins Applied Physics Laboratory, Laurel, MD, USA.
[20]Institut de Recherche en Astrophysique et Planétologie, Université Toulouse III Paul Sabatier, CNRS, CNES, Toulouse, France.
[21]Université Côte d'Azur, Observatoire de la Côte d'Azur, CNRS, IRD, Géoazur, Valbonne, France.
[22]Laboratoire de Météorologie Dynamique/IPSL, Sorbonne Université, CNRS, Ecole Normale Supérieure, PSL Research University, Ecole Polytechnique, Paris, France.

†Now at the Department of Earth, Atmospheric, and Planetary Sciences, Purdue University, Lafayette, IN, USA.

*Corresponding author. Email: posiolov@msss.com

Abstract: Two 130+ meter diameter impact craters formed on Mars during the later half of 2021. These are the two largest fresh impact craters discovered by the Mars Reconnaissance Orbiter since operations started 16 years ago. The impacts created two of the largest seismic events (magnitudes greater than 4) recorded by InSight during its three-year mission. The combination of orbital imagery and seismic ground motion enables the investigation of subsurface and atmospheric energy partitioning of the impact process on a planet with a thin atmosphere and the first direct test of Martian deep-interior seismic models with known event distances. The impact at 35°N excavated blocks of water ice, which is the lowest latitude ice has been directly observed on Mars.

One-Sentence Summary: Imaging and seismic recordings of meteoritic impacts on Mars help evaluate impact dynamics and deep-interior seismic models.

Main Text:

Seismic recordings of hypervelocity impacts (>3 km/s) are rare despite being the most common terrain modification process in the solar system. Earth is shielded by its atmosphere, consequently there are few seismically recorded ground impacts, and meteoroids that do reach the ground usually travel at terminal subsonic velocity and only form small craters (*1*–*3*). The Apollo Passive Seismic Experiments on the Moon recorded ground motions from artificial impacts, but these had slow relative velocities (<2.6 km/s), with respect to typical impact velocities of comets or asteroids colliding with the Moon, and formed craters smaller than 30 m (*4*). Larger natural impacts on the Moon were detected but have not been associated with imaged craters (*4*, *5*), and all are expected to be smaller than 100 m in diameter (*6*). On Earth, a multitude of seismic events with known source locations, e.g., explosion sources, have been used extensively for evaluating seismic velocity models, even down to the Earth's core (*7*). In contrast, there were only a few confirmed seismic source locations on Mars (all impacts), but these were small (<12 m in diameter) and near InSight (<300 km) so the seismic paths only sampled the shallow crust (*8*). The two new impact craters reported here allow for the first time an evaluation of deep interior Mars global velocity models and observations of the dynamics of the hypervelocity impact process.

The notable impacts (Fig. 1) were discovered using the Mars Reconnaissance Orbiter's (MRO) Context Camera (CTX) (*9*) and the Seismic Experiment for Interior Structure (SEIS) (*10*) of the Interior Exploration on the Seismic Investigations, Geodesy and Heat Transport (InSight) mission (*11*). Our CTX team independently discovered the Amazonis crater that we associated with the S1094b event. The earlier S1000a event, based on similar seismic signature, was then used to direct a search with MRO cameras to find the Tempe impact crater site. Both impacts generated craters >130 meters in diameter making them the largest fresh craters identified since the beginning of the MRO mission 16 years ago. The seismic events have identifiable surface waves, distinguishing them from other recorded and analyzed events on Mars and indicating shallow sources (*12*). Before these events, surface waves had not been unambiguously identified on any terrestrial planet other than Earth. The closer impact (ID S1094b) occurred at a distance of 58.5° (3,460 km) from the InSight lander on 24 December 2021 and formed the larger of the two craters (150±10 m in diameter). The other impact (ID S1000a) occurred at a distance of 126° (7,455 km) on 18 September 2021 and formed a cluster of craters (largest 130±12 m in diameter). The formation of the craters was time constrained using the MRO Mars Color Imager (MARCI) (*13*) to within a day (Table S1) making the association with the seismic events highly probable. The seismic events associated with the impacts have similar characteristics, both with approximately 4.0 magnitudes (Table S1, S2). Because the seismic waves traveled deep in the mantle, both events are critical for analysis of mantle velocity models. However, due to S1000a event's large distance, direct seismic waves are eclipsed by Mars's core (*14*) and more complex bouncing seismic body wave phases (PP, SS) were detected (Fig. S1). The additional attenuation and scattering experienced by these waves obscure the source characteristics. This makes source analysis much more challenging. In addition, the S1000a associated crater is located on the side of a graben (Fig. S2), which perturbed the blast pattern and prevented an easy identification of impactor parameters. In contrast, the closer impact (S1094b) occurred in a flat, dust covered region. Below, we first analyze the impact process for this closer impact before considering the implications for Mars interior models of both impacts.

One of the remarkable features of the S1094b impact was the prominent surface albedo disturbances it caused allowing for the estimation of ephemeral events that would otherwise be unknown, such as the impactor trajectory and the extent of atmospheric blast waves (Fig. 2, Fig. S3). The bearing of the bolide was estimated to be 60°±5° clockwise from north based on measuring the up-range "forbidden zone" (*15*) in the albedo ray pattern, and a down-range extended cluster of secondary impacts. We infer that the impactor approached the surface at an elevation angle of approximately 30° from horizontal. A steeper angle requires the asymmetric ejecta pattern to be muted, and a much shallower angle should have led to an elliptical crater planform (*15*, *16*). Two distinct arcuate rays ("scimitars") extending approximately northwest and south of the impact site likely formed from the superposition of two atmospheric blast waves disturbing surface dust: one generated by the passage of the meteoroid through the atmosphere (Mach cone) and the other by the ground impact (*17*), thus indicating both blast waves extended to at least 18 km laterally. These arcuate rays provide an independent though consistent measure of the impactor trajectory (56°). The meteoroid struck the surface at 18:49 LMST (Local Mean Solar Time) thus impacting on the orbital trailing side of Mars. We estimate the radial extent of surface dust disturbance from the crater to be 9 km (Fig. S3). This limit is consistent with the atmospheric blast pressure produced by a 0.1–1 kiloton (4×10^{11}–4×10^{12} J) surface explosive source (Fig. S4). The size of the atmospheric blast allows us to evaluate its contribution to the seismic signal.

Crater size is an important quantity for estimating the kinetic energy and momentum of the impactor for use in numerical models. An image from another camera on MRO, the High Resolution Imaging Science Experiment (HiRISE) (*18*), revealed more details of the crater and its immediate surroundings (Fig. 2). The crater is irregular in shape with an estimated rim-to-rim diameter of 150±10 meters. The depth of the crater floor to the crater rim based on photogrammetry results using HiRISE stereo images is roughly 21 meters. The abundant craters surrounding the new impact are likely almost all secondaries generated by this primary impactor as in comparison areas far (>10–20 km) from the new impact have few small craters. The bright patches and blocks surrounding the crater reveal that it excavated water ice from the subsurface at a lower latitude (35°N) than any prior ice-exposing crater (39°N) (*19*).

The geological context from orbital imagery aids in determining the appropriate physical models to use in numerical calculations. The S1094b crater is in the Amazonis Planitia region in an area of rugged volcanic plains (*20*) with CTX images showing lava-flow morphologies mantled by a modest cover of debris. This indicates that a target ground with properties of porous fractured basalt is appropriate for modeling the surface impact. To account for a harder rock site at the crater compared to the region around InSight, we use a local subsurface velocity model based on terrestrial lava flows (*21*) extrapolated to Mars surface conditions (*22*, *23*) (Fig. S5; Fig. S6) for seismic modeling.

The seismic source duration for an impact of this size is expected to be shorter than the crater formation timescale and limited to the duration of the non-linear shock wave propagation regime (*6*). The seismic event, S1094b, has a very broad frequency content and relatively flat spectra, from 0.1 Hz to 3 Hz (Fig. 3) with a signal lasting over 100 minutes (*24*) due to propagation coda (*25*). The event has an impulsive first arrival P-wave (1-sec uncertainty), followed by an emergent strong S-wave 6 min later (20-sec uncertainty). The third wave observed, arriving 8 min later, is a Rayleigh surface wave, expressed as a long-period dispersed pulse with 8–15 sec period (*12*). All body wave phases are characterized by a long

coda, indicative of strong scattering due to a near-surface source. The spectra display unusually high corner frequencies (3 Hz) compared to most other seismic events recorded on Mars. Shock physics modeling of the impact in a porous fractured basalt target (Fig. 4) indicates that most of the seismic moment is contained within a few hundred meters of the impact (orange bar in Fig. 4A). The moment release occurs over a short time period consistent with the cutoff frequency of 3 Hz identified in the P-wave displacement spectrum (Fig. 3D). Above the cutoff frequency, the amplitude shows a cubed frequency drop-off, as also observed for closer, smaller impacts on Mars (*8*) and for shallow explosions on Earth (*26*, *27*).

Seismic moment (M_0) is the key quantity that links the orbital observations of the impact and the impactor parameters to the seismic observations. For S1094b, the seismic moment estimate from S-body waves was originally calculated assuming a marsquake at 50±30 km depth to be 1.3×10^{15} Nm. (*28*). However, the impact seismic source deposits its energy at much shallower depths, in the strongly shocked region, estimated to be between 17- and 120-m depth from impact modeling, or approximately 50 m (Fig. 4B). We use our lava-flow seismic velocity model to conclude that the moment of a source at this depth is about 100 times smaller than a corresponding deep-crustal source for the same observed amplitude (Fig. 4A; Fig. S5). This is comparable to the seismic moment estimated from surface wave spectra, $M_0 = 7.5\times10^{13}$ Nm, at the same source depth (Fig. S7).

Empirical and numerical models were used to compute seismic moments for S1094b based on the observed crater size. The imaged crater diameter of 150±10 m corresponds to a vertical impactor momentum of $3.3\pm1.4\times10^{9}$ Ns based on empirical crater-scaling relationships and impactor mass, angle, and velocity probability distributions (Fig. S8; Fig. S9). For these values, numerical simulations predict seismic moments of $0.5–1.2\times10^{13}$ Nm for impacts in regolith and $2.8–7\times10^{13}$ Nm for fractured rock conditions (*29*, *30*). These estimates are consistent with the observed seismic moment corrected for relevant depths in our subsurface model (Fig. 4A). The seismic efficiency was estimated to be 10^{-5} based on scaling relations between seismic moment and crater diameter (*31*) with an order of magnitude uncertainty. This is lower than values estimated for lunar and Earth analogues (*32*), but larger than that previously modeled for small martian impact craters (*29*).

The extensive blast pattern around the S1094b crater suggests some of the seismic energy may also originate from energy released in the atmosphere and then coupled to the ground. Numerical impact simulations suggest that up to 10% of the impact energy is partitioned into kinetic energy on the planetary surface, primarily in the ejecta (*33*). For impact scenarios on Mars similar to S1094b, simulations with an atmosphere further suggest about 5% of the impact energy is partitioned into the blastwave (*34*). For an estimated impact energy of $1–8\times10^{13}$ J (Fig. S4), this could produce an atmospheric blast comparable to a 0.1–1 kT ($4\times10^{11}–4\times10^{12}$ J) surface explosion. Therefore, both seismic and image observations are consistent with such a blast and provide coherent constraints in time and space respectively. Semi-empirical airblast theory (*35*) extrapolated to Mars suggests such a blast would transition from the strong shock regime after 0.2–0.4 sec, which is consistent with the observed ~3 Hz P-wave cut-off frequency. The induced blast pressure is sufficient to mobilize surface dust to a radius of ~10 km, which is consistent with the observed disturbed dust pattern (Fig. 1; Fig. S3; Fig. S4). The estimated blast energy translates to an atmospheric moment $M_0 \approx (\gamma\text{-}1)E = 0.1–1.3\times10^{12}$ Nm, where γ is the adiabatic index (1.33 for Mars) and E is the blast energy (*36*). This is remarkably consistent with the moment-depth model when

extrapolated to the surface (Fig. 4A), implying that a moment of only 10^{12} Nm released in the atmosphere could explain a substantial part of the seismic body wave signal, with the remaining part coming from direct coupling of the impactor with the ground.

On Earth, atmospheric explosions easily excite surface waves (SW) (*37*) and are highly sensitive to burst altitude (*38*). Coupled solid/atmospheric Mars Rayleigh modes (*14*, *39*) are predicted to have excitation coefficients up to 10 times larger for a near-surface atmospheric source compared to one 50 m below the subsurface (Fig. S7). They are expected to have an increase in the excitation coefficients between 0.1 Hz and 0.15 Hz for sources above 50 meter altitude. This is not observed in the estimated S1094b spectra, and may be due to attenuation and scattering, which is not unexpected since scattering effects are predicted to generate increasing attenuation of surface waves with frequency on the Moon and Mars (*40*). Comparison of S1094b SW spectra with near surface excitation coefficients (Fig. S7) suggests that a portion of the SW signal could have originated from the blast just above the surface.

The Marsquake Service (MQS) (*41*) using SEIS data (*24*) estimated the seismic locations for both events (S1094b and S1000a). The distance to the events is determined using S-minus-P arrival times (SS-minus-PP for S1000a) (*42*, *43*) and polarization measurements of P and Rayleigh waves (PP for S1000a) (*12*). For the closer event (S1094b), the epicentral distance from the InSight lander was estimated to be 59.7°±6.1° (3,530±360 km), as compared to the actual distance of 58.5° (3460 km), a difference of only 70 km. For the second impact, S1000a, the distance was estimated at 128.3°±19° (7,591±1240 km), as compared to the actual distance of 126.1°, a difference of 130 km. Additional source parameters for these events are detailed in Tables S1 and S2.

The close agreement between distance estimates and the imaged locations increases our confidence in the Martian seismic velocity models (*44–48*) for the regions sampled by the direct body waves (Fig. S10). In particular, the models indicate the absence of mantle discontinuities in the 600 to 700 km depth range, which is the depth at which the P, S, PP, and SS waves turn (*44*). For the S1000a event, the P_{diff} phase, the P wave that diffracts along the core mantle boundary (CMB), has been tentatively identified (*14*). The PP-P_{diff} travel time difference is sensitive to lower mantle P-velocities below 800 km. Current models at these depths are constrained by core reflected S phases and the mineral-physics-based V_P/V_S ratio (Fig. S10). The observed PP-P_{diff} does not match the predicted values based on these models. This implies that either the P-velocities at the CMB need adjustment, or the V_P/V_S ratio in the lower mantle is different from current predictions. These two events act as calibrated measurements and help select among various Martian interior seismic velocity models (*44–48*); they corroborate Mars mantle velocity models to 800 km depth and will help to improve future models down to the CMB.

The first two recorded teleseismic events on Mars with orbital ground-truth observations have been used to constrain Martian interior seismic velocity models and infer dynamic impact processes including seismic moment release, impact source duration, and atmosphere-subsurface energy partitioning. The success in observing the formation of impact craters on Mars using instruments on several missions opens up a more detailed understanding of impact dynamics, atmospheric physics, and the exploration of planetary interiors.

References and Notes

1. W. N. Edwards, D. W. Eaton, P. G. Brown, Seismic observations of meteors: Coupling

theory and observations. *Rev. Geophys.* **46** (2008), doi:10.1029/2007RG000253.

2. P. Brown, D. O. ReVelle, E. A. Silber, W. N. Edwards, S. Arrowsmith, L. E. Jackson Jr., G. Tancredi, D. Eaton, Analysis of a crater-forming meteorite impact in Peru. *J. Geophys. Res. Planets*. **113** (2008), doi:10.1029/2008JE003105.
3. E. Gnos, B. A. Hofmann, M. A. Halawani, Y. Tarabulsi, M. Hakeem, M. Al Shanti, N. D. Greber, S. Holm, C. Alwmark, R. C. Greenwood, K. Ramseyer, The Wabar impact craters, Saudi Arabia, revisited. *Meteorit. Planet. Sci.* **48**, 2000–2014 (2013), doi:10.1111/maps.12218.
4. Y. Nakamura, G. V. Latham, H. J. Dorman, Apollo Lunar Seismic Experiment—Final summary. *J. Geophys. Res. Solid Earth*. **87**, A117–A123 (1982), doi:10.1029/JB087iS01p0A117.
5. P. Lognonné, C. L. Johnson, "Planetary Seismology" in *Treatise on Geophysics: Second Edition* (2015), pp. 65–120.
6. T. V. Gudkova, Ph. Lognonné, J. Gagnepain-Beyneix, Large impacts detected by the Apollo seismometers: Impactor mass and source cutoff frequency estimations. *Icarus*. **211**, 1049–1065 (2011), doi:10.1016/j.icarus.2010.10.028.
7. W. Wang, J. E. Vidale, Seismological observation of Earth's oscillating inner core. *Sci. Adv.* **8**, eabm9916 (2022), doi:10.1126/sciadv.abm9916.
8. R. F. Garcia, I. J. Daubar, E. Beucler, L. V. Posiolova, G. S. Collins, P. Lognonné, L. Rolland, Z. Xu, N. Wojcicka, A. Spiga, B. Fernando, G. Speth, L. Martire, A. Rajšić, K. Miljkovic, E. Sansom, C. Charalambous, S. Ceylan, S. Menina, L. Margerin, R. Lapeyre, T. Neidhart, N. A. Teanby, N. C. Schmerr, M. Bonnin, M. Froment, J. F. Clinton, Ö. Karatekin, S. C. Stähler, N. L. Dahmen, C. Duran, A. C. Horleston, T. Kawamura, M. Plasman, G. Zenhäusern, D. Giardini, M. P. Panning, M. C. Malin, W. B. Banerdt, Newly formed craters on Mars located using seismic and acoustic wave data from InSight. *Nat. Geosci.* (2022), doi:10.1038/s41561-022-01014-0.
9. M. C. Malin, J. F. Bell III, B. A. Cantor, M. A. Caplinger, W. M. Calvin, R. T. Clancy, K. S. Edgett, L. Edwards, R. M. Haberle, P. B. James, S. W. Lee, M. A. Ravine, P. C. Thomas, M. J. Wolff, Context Camera Investigation on board the Mars Reconnaissance Orbiter. *J. Geophys. Res. Planets*. **112** (2007), doi:10.1029/2006JE002808.
10. P. Lognonné, W. B. Banerdt, D. Giardini, W. T. Pike, U. Christensen, P. Laudet, S. de Raucourt, P. Zweifel, S. Calcutt, M. Bierwirth, K. J. Hurst, F. Ijpelaan, J. W. Umland, R. Llorca-Cejudo, S. A. Larson, R. F. Garcia, S. Kedar, B. Knapmeyer-Endrun, D. Mimoun, A. Mocquet, M. P. Panning, R. C. Weber, A. Sylvestre-Baron, G. Pont, N. Verdier, L. Kerjean, L. J. Facto, V. Gharakanian, J. E. Feldman, T. L. Hoffman, D. B. Klein, K. Klein, N. P. Onufer, J. Paredes-Garcia, M. P. Petkov, J. R. Willis, S. E. Smrekar, M. Drilleau, T. Gabsi, T. Nebut, O. Robert, S. Tillier, C. Moreau, M. Parise, G. Aveni, S. Ben Charef, Y. Bennour, T. Camus, P. A. Dandonneau, C. Desfoux, B. Lecomte, O. Pot, P. Revuz, D. Mance, J. tenPierick, N. E. Bowles, C. Charalambous, A. K. Delahunty, J. Hurley, R. Irshad, H. Liu, A. G. Mukherjee, I. M. Standley, A. E. Stott, J. Temple, T. Warren, M. Eberhardt, A. Kramer, W. Kühne, E.-P. Miettinen, M. Monecke, C. Aicardi, M. André, J. Baroukh, A. Borrien, A. Bouisset, P. Boutte, K. Brethomé, C. Brysbaert, T. Carlier, M. Deleuze, J. M. Desmarres, D. Dilhan, C. Doucet, D. Faye, N. Faye-Refalo, R. Gonzalez, C. Imbert, C. Larigauderie, E. Locatelli, L. Luno, J.-R. Meyer, F. Mialhe, J. M. Mouret, M. Nonon, Y. Pahn, A. Paillet, P.

Pasquier, G. Perez, R. Perez, L. Perrin, B. Pouilloux, A. Rosak, I. Savin de Larclause, J. Sicre, M. Sodki, N. Toulemont, B. Vella, C. Yana, F. Alibay, O. M. Avalos, M. A. Balzer, P. Bhandari, E. Blanco, B. D. Bone, J. C. Bousman, P. Bruneau, F. J. Calef, R. J. Calvet, S. A. D'Agostino, G. de los Santos, R. G. Deen, R. W. Denise, J. Ervin, N. W. Ferraro, H. E. Gengl, F. Grinblat, D. Hernandez, M. Hetzel, M. E. Johnson, L. Khachikyan, J. Y. Lin, S. M. Madzunkov, S. L. Marshall, I. G. Mikellides, E. A. Miller, W. Raff, J. E. Singer, C. M. Sunday, J. F. Villalvazo, M. C. Wallace, D. Banfield, J. A. Rodriguez-Manfredi, C. T. Russell, A. Trebi-Ollennu, J. N. Maki, E. Beucler, M. Böse, C. Bonjour, J. L. Berenguer, S. Ceylan, J. Clinton, V. Conejero, I. Daubar, V. Dehant, P. Delage, F. Euchner, I. Estève, L. Fayon, L. Ferraioli, C. L. Johnson, J. Gagnepain-Beyneix, M. Golombek, A. Khan, T. Kawamura, B. Kenda, P. Labrot, N. Murdoch, C. Pardo, C. Perrin, L. Pou, A. Sauron, D. Savoie, S. Stähler, E. Stutzmann, N. A. Teanby, J. Tromp, M. van Driel, M. Wieczorek, R. Widmer-Schnidrig, J. Wookey, SEIS: Insight's Seismic Experiment for Internal Structure of Mars. *Space Sci. Rev.* **215**, 12 (2019), doi:10.1007/s11214-018-0574-6.

11. W. B. Banerdt, S. E. Smrekar, D. Banfield, D. Giardini, M. Golombek, C. L. Johnson, P. Lognonné, A. Spiga, T. Spohn, C. Perrin, S. C. Stähler, D. Antonangeli, S. Asmar, C. Beghein, N. Bowles, E. Bozdag, P. Chi, U. Christensen, J. Clinton, G. S. Collins, I. Daubar, V. Dehant, M. Drilleau, M. Fillingim, W. Folkner, R. F. Garcia, J. Garvin, J. Grant, M. Grott, J. Grygorczuk, T. Hudson, J. C. E. Irving, G. Kargl, T. Kawamura, S. Kedar, S. King, B. Knapmeyer-Endrun, M. Knapmeyer, M. Lemmon, R. Lorenz, J. N. Maki, L. Margerin, S. M. McLennan, C. Michaut, D. Mimoun, A. Mittelholz, A. Mocquet, P. Morgan, N. T. Mueller, N. Murdoch, S. Nagihara, C. Newman, F. Nimmo, M. Panning, W. T. Pike, A.-C. Plesa, S. Rodriguez, J. A. Rodriguez-Manfredi, C. T. Russell, N. Schmerr, M. Siegler, S. Stanley, E. Stutzmann, N. Teanby, J. Tromp, M. van Driel, N. Warner, R. Weber, M. Wieczorek, Initial results from the InSight mission on Mars. *Nat. Geosci.* **13**, 183–189 (2020), doi:10.1038/s41561-020-0544-y.

12. D. Kim, W. B. Banerdt, S. Ceylan, D. Giardini, V. Lekic, P. Lognonné, C. Beghein, É. Beucler, S. Carrasco, C. Charalambous, J. Clinton, M. Drilleau, C. Duran, M. P. Golombek, R. Joshi, A. Khan, B. Knapmeyer-Endrun, J. Li, R. Maguire, W. T. Pike, H. Samuel, M. Schimmel, N. Schmerr, S. C. Stähler, É. Stutzmann, M. A. Wieczorek, Z. Xu, A. Batov, E. Bozdag, N. Dahmen, P. M. Davis, T. Gudkova, A. Horleston, Q. Huang, T. Kawamura, S. King, S. M. McLennan, F. Nimmo, M. Plasman, A.-C. Plesa, I. E. Stepanova, E. Weidner, G. Zenhäusern, I. J. Daubar, B. Fernando, R. F. Garcia, L. V. Posiolova, M. P. Panning, Surface waves and crustal structure on Mars. *Science*. **in revision** (2022).

13. J. F. Bell, M. J. Wolff, M. C. Malin, W. M. Calvin, B. A. Cantor, M. A. Caplinger, R. T. Clancy, K. S. Edgett, L. J. Edwards, J. Fahle, F. Ghaemi, R. M. Haberle, A. Hale, P. B. James, S. W. Lee, T. McConnochie, E. Noe Dobrea, M. A. Ravine, D. Schaeffer, K. D. Supulver, P. C. Thomas, Mars Reconnaissance Orbiter Mars Color Imager (MARCI): Instrument description, calibration, and performance. *J. Geophys. Res. Planets*. **114** (2009), doi:10.1029/2008JE003315.

14. A. C. Horleston, J. F. Clinton, S. Ceylan, D. Giardini, C. Charalambous, J. C. E. Irving, P. Lognonné, S. C. Stähler, G. Zenhäusern, N. L. Dahmen, C. Duran, T. Kawamura, A. Khan, D. Kim, M. Plasman, F. Euchner, C. Beghein, É. Beucler, Q. Huang, M. Knapmeyer, B. Knapmeyer-Endrun, V. Lekić, J. Li, C. Perrin, M. Schimmel, N. C. Schmerr, A. E. Stott, E. Stutzmann, N. A. Teanby, Z. Xu, M. Panning, W. B. Banerdt, The Far Side of Mars: Two Distant Marsquakes Detected by InSight. *Seism. Rec.* **2**, 88–99 (2022),

doi:10.1785/0320220007.

15. D. E. Gault, J. A. Wedekind, Experimental studies of oblique impact. *Lunar Planet. Sci. Conf. Proc.* **3**, 3843–3875 (1978).

16. D. Elbeshausen, K. Wünnemann, G. S. Collins, The transition from circular to elliptical impact craters. *J. Geophys. Res. Planets*. **118**, 2295–2309 (2013), doi:10.1002/2013JE004477.

17. B. Ivanov, G. Barnes, I. Daubar, C. Dundas, A. McEwen, J. Melosh, New craters on Mars: Air shock wave traces, 4212 (2020), doi:10.5194/egusphere-egu2020-4212.

18. A. S. McEwen, E. M. Eliason, J. W. Bergstrom, N. T. Bridges, C. J. Hansen, W. A. Delamere, J. A. Grant, V. C. Gulick, K. E. Herkenhoff, L. Keszthelyi, R. L. Kirk, M. T. Mellon, S. W. Squyres, N. Thomas, C. M. Weitz, Mars Reconnaissance Orbiter's High Resolution Imaging Science Experiment (HiRISE). *J. Geophys. Res. Planets*. **112** (2007), doi:10.1029/2005JE002605.

19. C. M. Dundas, M. T. Mellon, S. J. Conway, I. J. Daubar, K. E. Williams, L. Ojha, J. J. Wray, A. M. Bramson, S. Byrne, A. S. McEwen, L. V. Posiolova, G. Speth, D. Viola, M. E. Landis, G. A. Morgan, A. V. Pathare, Widespread Exposures of Extensive Clean Shallow Ice in the Midlatitudes of Mars. *J. Geophys. Res. Planets*. **126**, e2020JE006617 (2021), doi:10.1029/2020JE006617.

20. K. L. Tanaka, J. Skinner Jr, J. Dohm, R. P. III, E. J. Kolb, C. M. Fortezzo, T. Platz, G. G. Michael, T. Hare, Geologic Map of Mars. *Sci. Investig. Map*. **3292** (2014), doi:10.3133/sim3292.

21. P. Lesage, M. J. Heap, A. Kushnir, A generic model for the shallow velocity structure of volcanoes. *J. Volcanol. Geotherm. Res.* **356**, 114–126 (2018), doi:10.1016/j.jvolgeores.2018.03.003.

22. C. Larmat, K. Onodera, R. Maguire, P. Lognonné, Modelling to resolve whether SEIS, the seismometer of the NASA Insight lander, has detected the formation of a 1.5m diameter crater which occurred about 40km away. (2020), doi:10.18715/JGR_NEWCRATERMOD_2020.

23. I. J. Daubar, P. Lognonné, N. A. Teanby, G. S. Collins, J. Clinton, S. Stähler, A. Spiga, F. Karakostas, S. Ceylan, M. Malin, A. S. McEwen, R. Maguire, C. Charalambous, K. Onodera, A. Lucas, L. Rolland, J. Vaubaillon, T. Kawamura, M. Böse, A. Horleston, M. van Driel, J. Stevanović, K. Miljković, B. Fernando, Q. Huang, D. Giardini, C. S. Larmat, K. Leng, A. Rajšić, N. Schmerr, N. Wójcicka, T. Pike, J. Wookey, S. Rodriguez, R. Garcia, M. E. Banks, L. Margerin, L. Posiolova, B. Banerdt, A New Crater Near InSight: Implications for Seismic Impact Detectability on Mars. *J. Geophys. Res. Planets*. **125**, e2020JE006382 (2020), doi:10.1029/2020JE006382.

24. InSight Mars SEIS Data Service, SEIS raw data, Insight Mission, IPGP, JPL, CNES, ETHZ, ICL, MPS, ISAE-Supaero, LPG, MFSC. (2019), doi:10.18715/SEIS.INSIGHT.XB_2016.

25. P. Lognonné, W. B. Banerdt, W. T. Pike, D. Giardini, U. Christensen, R. F. Garcia, T. Kawamura, S. Kedar, B. Knapmeyer-Endrun, L. Margerin, F. Nimmo, M. Panning, B. Tauzin, J.-R. Scholz, D. Antonangeli, S. Barkaoui, E. Beucler, F. Bissig, N. Brinkman, M. Calvet, S. Ceylan, C. Charalambous, P. Davis, M. van Driel, M. Drilleau, L. Fayon, R. Joshi, B. Kenda, A. Khan, M. Knapmeyer, V. Lekic, J. McClean, D. Mimoun, N. Murdoch, L. Pan,

C. Perrin, B. Pinot, L. Pou, S. Menina, S. Rodriguez, C. Schmelzbach, N. Schmerr, D. Sollberger, A. Spiga, S. Stähler, A. Stott, E. Stutzmann, S. Tharimena, R. Widmer-Schnidrig, F. Andersson, V. Ansan, C. Beghein, M. Böse, E. Bozdag, J. Clinton, I. Daubar, P. Delage, N. Fuji, M. Golombek, M. Grott, A. Horleston, K. Hurst, J. Irving, A. Jacob, J. Knollenberg, S. Krasner, C. Krause, R. Lorenz, C. Michaut, R. Myhill, T. Nissen-Meyer, J. ten Pierick, A.-C. Plesa, C. Quantin-Nataf, J. Robertsson, L. Rochas, M. Schimmel, S. Smrekar, T. Spohn, N. Teanby, J. Tromp, J. Vallade, N. Verdier, C. Vrettos, R. Weber, D. Banfield, E. Barrett, M. Bierwirth, S. Calcutt, N. Compaire, C. L. Johnson, D. Mance, F. Euchner, L. Kerjean, G. Mainsant, A. Mocquet, J. A. Rodriguez Manfredi, G. Pont, P. Laudet, T. Nebut, S. de Raucourt, O. Robert, C. T. Russell, A. Sylvestre-Baron, S. Tillier, T. Warren, M. Wieczorek, C. Yana, P. Zweifel, Constraints on the shallow elastic and anelastic structure of Mars from InSight seismic data. *Nat. Geosci.* **13**, 213–220 (2020), doi:10.1038/s41561-020-0536-y.

26. W. R. Walter, K. F. Priestley, "High-Frequency P Wave Spectra from Explosions and Earthquakes" in *Explosion Source Phenomenology* (American Geophysical Union (AGU), 1991; https://onlinelibrary.wiley.com/doi/abs/10.1029/GM065p0219), pp. 219–228.

27. S. R. Ford, W. R. Walter, S. D. Ruppert, E. M. Matzel, T. F. Hauk, R. Gok, "Toward an Empirically-Based Parametric Explosion Spectral Model" (LAWRENCE LIVERMORE NATIONAL LAB CA, 2011), (available at https://apps.dtic.mil/sti/citations/ADA568895).

28. M. Böse, S. C. Stähler, N. Deichmann, D. Giardini, J. Clinton, P. Lognonné, S. Ceylan, M. van Driel, C. Charalambous, N. Dahmen, A. Horleston, T. Kawamura, A. Khan, M. Knapmeyer, G. Orhand□Mainsant, J. Scholz, F. Euchner, W. B. Banerdt, Magnitude Scales for Marsquakes Calibrated from InSight Data. *Bull. Seismol. Soc. Am.* **111**, 3003–3015 (2021), doi:10.1785/0120210045.

29. N. Wójcicka, G. S. Collins, I. D. Bastow, N. A. Teanby, K. Miljković, A. Rajšić, I. Daubar, P. Lognonné, The Seismic Moment and Seismic Efficiency of Small Impacts on Mars. *J. Geophys. Res. Planets*. **125**, e2020JE006540 (2020), doi:10.1029/2020JE006540.

30. A. Rajšić, K. Miljković, G. S. Collins, K. Wünnemann, I. J. Daubar, N. Wójcicka, M. A. Wieczorek, Seismic Efficiency for Simple Crater Formation in the Martian Top Crust Analog. *J. Geophys. Res. Planets*. **126**, e2020JE006662 (2021), doi:10.1029/2020JE006662.

31. N. A. Teanby, J. Wookey, Seismic detection of meteorite impacts on Mars. *Phys. Earth Planet. Inter.* (2011), doi:10.1016/j.pepi.2011.03.004.

32. I. Daubar, P. Lognonné, N. A. Teanby, K. Miljkovic, J. Stevanović, J. Vaubaillon, B. Kenda, T. Kawamura, J. Clinton, A. Lucas, M. Drilleau, C. Yana, G. S. Collins, D. Banfield, M. Golombek, S. Kedar, N. Schmerr, R. Garcia, S. Rodriguez, T. Gudkova, S. May, M. Banks, J. Maki, E. Sansom, F. Karakostas, M. Panning, N. Fuji, J. Wookey, M. van Driel, M. Lemmon, V. Ansan, M. Böse, S. Stähler, H. Kanamori, J. Richardson, S. Smrekar, W. B. Banerdt, Impact-Seismic Investigations of the InSight Mission. *Space Sci. Rev.* **214**, 132 (2018), doi:10.1007/s11214-018-0562-x.

33. J. D. Okeefe, T. J. Ahrens, Impact-induced energy partitioning, melting, and vaporization on terrestrial planets. *Lunar Planet. Sci. Conf. Proc.* **3**, 3357–3374 (1977).

34. I. V. Nemtchinov, V. V. Shuvalov, R. Greeley, Impact-mobilized dust in the Martian atmosphere. *J. Geophys. Res. Planets*. **107**, 17-1-17–8 (2002), doi:10.1029/2001JE001834.

35. S. Glasstone, P. J. Dolan, "The Effects of Nuclear Weapons. Third edition" (Department of

Defense, Washington, D.C. (USA); Department of Energy, Washington, D.C. (USA), 1977), p. 662, (available at https://doi.org/10.2172/6852629).

36. P. Lognonné, B. Mosser, F. A. Dahlen, Excitation of Jovian Seismic Waves by the Shoemaker-Levy 9 Cometary Impact. *Icarus*. **110**, 180–195 (1994), doi:10.1006/icar.1994.1115.

37. M. N. Toksöz, A. Ben-Menahem, Excitation of seismic surface waves by atmospheric nuclear explosions. *J. Geophys. Res. 1896-1977*. **69**, 1639–1648 (1964), doi:10.1029/JZ069i008p01639.

38. D. G. Harkrider, C. A. Newton, E. A. Flinn, Theoretical Effect of Yield and Burst Height of Atmospheric Explosions on Rayleigh Wave Amplitudes. *Geophys. J. Int.* **36**, 191–225 (1974), doi:10.1111/j.1365-246X.1974.tb03632.x.

39. P. Lognonné, F. Karakostas, L. Rolland, Y. Nishikawa, Modeling of atmospheric-coupled Rayleigh waves on planets with atmosphere: From Earth observation to Mars and Venus perspectives. *J. Acoust. Soc. Am.* **140**, 1447 (2016), doi:10.1121/1.4960788.

40. K. Onodera, T. Kawamura, S. Tanaka, Y. Ishihara, T. Maeda, Numerical Simulation of Lunar Seismic Wave Propagation: Investigation of Subsurface Scattering Properties Near Apollo 12 Landing Site. *J. Geophys. Res. Planets*. **126**, e2020JE006406 (2021), doi:10.1029/2020JE006406.

41. InSight Marsquake Service, Mars Seismic Catalogue, InSight Mission; V9 2022-01-01 (2022), doi:10.12686/A14.

42. M. Böse, J. F. Clinton, S. Ceylan, F. Euchner, M. van Driel, A. Khan, D. Giardini, P. Lognonné, W. B. Banerdt, A probabilistic framework for single-station location of seismicity on Earth and Mars. *Phys. Earth Planet. Inter.* **262**, 48–65 (2017), doi:10.1016/j.pepi.2016.11.003.

43. J. F. Clinton, S. Ceylan, M. van Driel, D. Giardini, S. C. Stähler, M. Böse, C. Charalambous, N. L. Dahmen, A. Horleston, T. Kawamura, A. Khan, G. Orhand-Mainsant, J.-R. Scholz, F. Euchner, W. B. Banerdt, P. Lognonné, D. Banfield, E. Beucler, R. F. Garcia, S. Kedar, M. P. Panning, C. Perrin, W. T. Pike, S. E. Smrekar, A. Spiga, A. E. Stott, The Marsquake catalogue from InSight, sols 0–478. *Phys. Earth Planet. Inter.* **310**, 106595 (2021), doi:10.1016/j.pepi.2020.106595.

44. C. Durán, A. Khan, S. Ceylan, G. Zenhäusern, S. Stähler, J. F. Clinton, D. Giardini, Seismology on Mars: An analysis of direct, reflected, and converted seismic body waves with implications for interior structure. *Phys. Earth Planet. Inter.* **325**, 106851 (2022), doi:10.1016/j.pepi.2022.106851.

45. S. C. Stähler, A. Khan, W. B. Banerdt, P. Lognonné, D. Giardini, S. Ceylan, M. Drilleau, A. C. Duran, R. F. Garcia, Q. Huang, D. Kim, V. Lekic, H. Samuel, M. Schimmel, N. Schmerr, D. Sollberger, É. Stutzmann, Z. Xu, D. Antonangeli, C. Charalambous, P. M. Davis, J. C. E. Irving, T. Kawamura, M. Knapmeyer, R. Maguire, A. G. Marusiak, M. P. Panning, C. Perrin, A.-C. Plesa, A. Rivoldini, C. Schmelzbach, G. Zenhäusern, É. Beucler, J. Clinton, N. Dahmen, M. van Driel, T. Gudkova, A. Horleston, W. T. Pike, M. Plasman, S. E. Smrekar, Seismic detection of the martian core. *Science*. **373**, 443–448 (2021), doi:10.1126/science.abi7730.

46. A. Khan, S. Ceylan, M. van Driel, D. Giardini, P. Lognonné, H. Samuel, N. C. Schmerr, S.

C. Stähler, A. C. Duran, Q. Huang, D. Kim, A. Broquet, C. Charalambous, J. F. Clinton, P. M. Davis, M. Drilleau, F. Karakostas, V. Lekic, S. M. McLennan, R. R. Maguire, C. Michaut, M. P. Panning, W. T. Pike, B. Pinot, M. Plasman, J.-R. Scholz, R. Widmer-Schnidrig, T. Spohn, S. E. Smrekar, W. B. Banerdt, Upper mantle structure of Mars from InSight seismic data. *Science*. **373**, 434–438 (2021), doi:10.1126/science.abf2966.

47. A. Khan, P. A. Sossi, C. Liebske, A. Rivoldini, D. Giardini, Geophysical and cosmochemical evidence for a volatile-rich Mars. *Earth Planet. Sci. Lett.* **578**, 117330 (2022), doi:10.1016/j.epsl.2021.117330.

48. M. Drilleau, H. Samuel, R. F. Garcia, A. Rivoldini, C. Perrin, C. Michaut, M. Wieczorek, B. Tauzin, J. A. D. Connolly, P. Meyer, P. Lognonné, W. B. Banerdt, Marsquake locations and 1-D seismic models for Mars from InSight data (2022), doi:10.1002/essoar.10511074.2.

49. M. C. Malin, K. S. Edgett, Mars Global Surveyor Mars Orbiter Camera: Interplanetary cruise through primary mission. *J. Geophys. Res. Planets*. **106**, 23429–23570 (2001), doi:10.1029/2000JE001455.

50. D. E. Smith, M. T. Zuber, H. V. Frey, J. B. Garvin, J. W. Head, D. O. Muhleman, G. H. Pettengill, R. J. Phillips, S. C. Solomon, H. J. Zwally, W. B. Banerdt, T. C. Duxbury, M. P. Golombek, F. G. Lemoine, G. A. Neumann, D. D. Rowlands, O. Aharonson, P. G. Ford, A. B. Ivanov, C. L. Johnson, P. J. McGovern, J. B. Abshire, R. S. Afzal, X. Sun, Mars Orbiter Laser Altimeter: Experiment summary after the first year of global mapping of Mars. *J. Geophys. Res. Planets*. **106**, 23689–23722 (2001), doi:10.1029/2000JE001364.

51. R. W. Zurek, S. E. Smrekar, An overview of the Mars Reconnaissance Orbiter (MRO) science mission. *J. Geophys. Res. Planets*. **112** (2007), doi:10.1029/2006JE002701.

52. D. Banfield, A. Spiga, C. Newman, F. Forget, M. Lemmon, R. Lorenz, N. Murdoch, D. Viudez-Moreiras, J. Pla-Garcia, R. F. Garcia, P. Lognonné, Ö. Karatekin, C. Perrin, L. Martire, N. Teanby, B. V. Hove, J. N. Maki, B. Kenda, N. T. Mueller, S. Rodriguez, T. Kawamura, J. B. McClean, A. E. Stott, C. Charalambous, E. Millour, C. L. Johnson, A. Mittelholz, A. Määttänen, S. R. Lewis, J. Clinton, S. C. Stähler, S. Ceylan, D. Giardini, T. Warren, W. T. Pike, I. Daubar, M. Golombek, L. Rolland, R. Widmer-Schnidrig, D. Mimoun, É. Beucler, A. Jacob, A. Lucas, M. Baker, V. Ansan, K. Hurst, L. Mora-Sotomayor, S. Navarro, J. Torres, A. Lepinette, A. Molina, M. Marin-Jimenez, J. Gomez-Elvira, V. Peinado, J.-A. Rodriguez-Manfredi, B. T. Carcich, S. Sackett, C. T. Russell, T. Spohn, S. E. Smrekar, W. B. Banerdt, The atmosphere of Mars as observed by InSight. *Nat. Geosci.* **13**, 190–198 (2020), doi:10.1038/s41561-020-0534-0.

53. G. Zenhäusern, S. C. Stähler, J. F. Clinton, D. Giardini, S. Ceylan, R. F. Garcia, Low frequency marsquakes and where to find them, Back Azimuth Determination Using a Polarization Analysis Approach (2022).

54. L. I. Sedov, Propagation of strong shock waves. *J. Appl. Math. Mech.* **10**, 241–250 (1946).

55. R. D. Lorenz, Vortex Encounter Rates with Fixed Barometer Stations: Comparison with Visual Dust Devil Counts and Large-Eddy Simulations. *J. Atmospheric Sci.* **71**, 4461–4472 (2014), doi:10.1175/JAS-D-14-0138.1.

56. R. Greeley, R. Leach, B. White, J. Iversen, J. B. Pollack, Threshold windspeeds for sand on Mars: Wind tunnel simulations. *Geophys. Res. Lett.* **7** (1980), doi:10.1029/GL007i002p00121.

57. K. Aki, P. G. Richards, *Quantitative Seismology* (University Science Books, 2002).

58. C. Larmat, K. Onodera, R. Maguire, P. Lognonné, Modelling to resolve whether SEIS, the seismometer of the NASA Insight lander, has detected the formation of a 1.5m diameter crater which occurred about 40km away. (2020), p. 8 MB, , doi:10.18715/JGR_NEWCRATERMOD_2020.

59. B. Knapmeyer-Endrun, M. P. Panning, F. Bissig, R. Joshi, A. Khan, D. Kim, V. Lekić, B. Tauzin, S. Tharimena, M. Plasman, N. Compaire, R. F. Garcia, L. Margerin, M. Schimmel, É. Stutzmann, N. Schmerr, E. Bozdağ, A.-C. Plesa, M. A. Wieczorek, A. Broquet, D. Antonangeli, S. M. McLennan, H. Samuel, C. Michaut, L. Pan, S. E. Smrekar, C. L. Johnson, N. Brinkman, A. Mittelholz, A. Rivoldini, P. M. Davis, P. Lognonné, B. Pinot, J.-R. Scholz, S. Stähler, M. Knapmeyer, M. van Driel, D. Giardini, W. B. Banerdt, Thickness and structure of the martian crust from InSight seismic data. *Science*. **373**, 438–443 (2021), doi:10.1126/science.abf8966.

60. A. A. Amsden, H. M. Ruppel, C. W. Hirt, SALE: a simplified ALE computer program for fluid flow at all speeds. *UNT Digit. Libr.* (1980), , doi:10.2172/5176006.

61. G. S. Collins, H. J. Melosh, B. A. Ivanov, Modeling damage and deformation in impact simulations. *Meteorit. Planet. Sci.* **39**, 217–231 (2004), doi:10.1111/j.1945-5100.2004.tb00337.x.

62. K. Wünnemann, G. S. Collins, H. J. Melosh, A strain-based porosity model for use in hydrocode simulations of impacts and implications for transient crater growth in porous targets. *Icarus*. **180**, 514–527 (2006), doi:10.1016/j.icarus.2005.10.013.

63. A. Rajšić, K. Miljković, N. Wójcicka, G. S. Collins, K. Onodera, T. Kawamura, P. Lognonné, M. A. Wieczorek, I. J. Daubar, Numerical Simulations of the Apollo S-IVB Artificial Impacts on the Moon. *Earth Space Sci.* **8**, e2021EA001887 (2021), doi:10.1029/2021EA001887.

64. G. G. Sorrells, J. A. McDonald, Z. A. Der, E. Herrin, Earth Motion Caused by Local Atmospheric Pressure Changes. *Geophys. J. Int.* **26**, 83–98 (1971), doi:10.1111/j.1365-246X.1971.tb03384.x.

65. É. Clévédé, P. Lognonné, "Higher order perturbation theory: 3D synthetic seismogram package" in *International Geophysics* (Elsevier, 2003), vol. 81, p. 1639.

66. F. Forget, F. Hourdin, R. Fournier, C. Hourdin, O. Talagrand, M. Collins, S. R. Lewis, P. L. Read, J.-P. Huot, Improved general circulation models of the Martian atmosphere from the surface to above 80 km. *J. Geophys. Res. Planets*. **104**, 24155–24175 (1999), doi:10.1029/1999JE001025.

67. E. Millour, F. Forget, A. Spiga, M. Vals, V. Zakharov, L. Montabone, "Mars climate database" in *From Mars Express to ExoMars, 27-28 February 2018, Madrid, Spain* (2018).

68. J. B. Plescia, M. S. Robinson, R. Wagner, R. Baldridge, Ranger and Apollo S-IVB spacecraft impact craters. *Planet. Space Sci.* **124** (2016), doi:10.1016/j.pss.2016.01.002.

69. K. Holsapple, K. Housen, A crater and its ejecta: An interpretation of Deep Impact. *Icarus*. **191**, 345–356 (2007), doi:10.1016/j.icarus.2006.08.029.

70. M. Le Feuvre, M. A. Wieczorek, Nonuniform cratering of the Moon and a revised crater chronology of the inner Solar System. *Icarus*. **214**, 1–20 (2011),

doi:10.1016/j.icarus.2011.03.010.

71. P. A. Bland, N. A. Artemieva, The rate of small impacts on Earth. *Meteorit. Planet. Sci.* **41**, 607–631 (2006), doi:10.1111/j.1945-5100.2006.tb00485.x.

72. E. M. Shoemaker, "Interpretation of Lunar Craters" in *Physics and Astronomy of the Moon*, Z. Kopal, Ed. (Academic Press, 1961; https://www.sciencedirect.com/science/article/pii/B9781483232409500122), pp. 283–359.

73. H. P. Crotwell, T. J. Owens, J. Ritsema, The TauP Toolkit: Flexible Seismic Travel-time and Ray-path Utilities. *Seismol. Res. Lett.* **70**, 154–160 (1999), doi:10.1785/gssrl.70.2.154.

74. M. A. Wieczorek, A. Broquet, S. M. McLennan, A. Rivoldini, M. Golombek, D. Antonangeli, C. Beghein, D. Giardini, T. Gudkova, S. Gyalay, C. L. Johnson, R. Joshi, D. Kim, S. D. King, B. Knapmeyer-Endrun, P. Lognonné, C. Michaut, A. Mittelholz, F. Nimmo, L. Ojha, M. P. Panning, A.-C. Plesa, M. A. Siegler, S. E. Smrekar, T. Spohn, W. B. Banerdt, InSight Constraints on the Global Character of the Martian Crust. *J. Geophys. Res. Planets*. **127**, e2022JE007298 (2022), doi:10.1029/2022JE007298.

Acknowledgments:

Any use of trade, firm, or product names is for descriptive purposes only and does not imply endorsement by the U.S. Government.

This is InSight contribution 221 and LA-UR-22-27122.

We acknowledge NASA, CNES, partner agencies and institutions (UKSA, SSO, DLR, JPL, IPGP-CNRS, ETHZ, ICL, MPS-MPG), and the operators of JPL, SISMOC, MSDS, IRIS-DMC and PDS for providing SEED SEIS data. This research was carried out in part at the Jet Propulsion Laboratory, California Institute of Technology, under a contract with the National Aeronautics and Space Administration (80NM0018D0004).

Funding:

NASA-NNN12AA01C with subcontract JPL-1515835 (LVP, MCM, BC, CK, GS, DS, AV, AW).

InSight PSP grant 80NSSC20K0971 (IJD).

The MRO HiRISE project (CMD)

Funding from ETH Zurich through the ETH+ funding scheme (ETH+02 19-1: “Planet Mars") (JC, DG, SC, SCS, CD, ND, AK, GZ).

ETH research grant ETH-10 17-3 (SCS).

UK Space Agency grants ST/R002096/1, ST/V00638X/1, ST/T002026/1, ST/S001514/1 and ST/W002523/1 (AH, CC, NAT, GSC, NW, WTP).

The Australian Research Council (DP180100661and FT210100063) (KM, AR).

This study contributes to the IdEx Université de Paris ANR-18-IDEX-0001 (PL, TK, MF, ZX, SM, CP, MP, MD).

The French Space Agency CNES and ANR fund (ANR-19-CE31-0008-08) (PL, TK, MF, XZ, EB, RG, LM, SM, CP, CP, MP, LR, AS, AS, MD)

Center for Space and Earth Science of LANL (Student Fellow Project) (MF, CL, ER)

Author contributions:

Lead of the CTX/imaging interpretation: LVP

Lead of the SEIS interpretation: PL

Text contributions: BF, ID, GSC, JFC, LVP, PL, SCS, TK, ZX

Edits to main text and supplementary material: BF, ID, MEB, RDL, SC, SCS

Figures contributions: AV, BAC, CK, GS, JFC, LVP, MCM, PL, SC, TK, MF

Data services: CP, FE

Geological interpretation: MEB, MG, MCM

Seismic analysis: AH, CC, CD, CP, DK, EB, GZ, JC, MD, MP, ND, PD, SC, SCS, TK, WTP

Seismic interpretation: AH, AK, DG, DK, JC, LM, MF, PD, SM, SCS, TK, WTP, ZX

Image analysis: AW, BAC, CMD, CK, DS, GS, ID, LVP, MCM

Targeting orbital assets: AW, CD, DS, GS, IJD, LVP

Seismic moment analysis: PL, TK, ZX

Impact model contribution and/or simulations: AR, CL, GSC, KM, NW, RDL

Seismo-atmosphere coupling work: AS, LR, MR, PL, TK

Seismic source modeling discussion: CL, ER, MF, NAT, PL

Seismic efficiency analysis: AS, NAT

Search for atmospheric signals: AS, PL, RFG

InSight mission management: WBB, MPP

SEIS instrument development and management: PL, DG, WTP, WBB

CTX/MARCI development: MCM

CTX/MARCI management: LVP

Competing interests: Authors declare that they have no competing interests.

Data and materials availability: MRO data are available from the NASA-PDS repository. The InSight event catalog and waveform data are available from the IRIS-DMC, NASA-PDS, SEIS-InSight data portal and IPGP data center.

Supplementary Materials

Materials and Methods

Figs. S1 to S10

Tables S1 to S2

References (*51–74*)

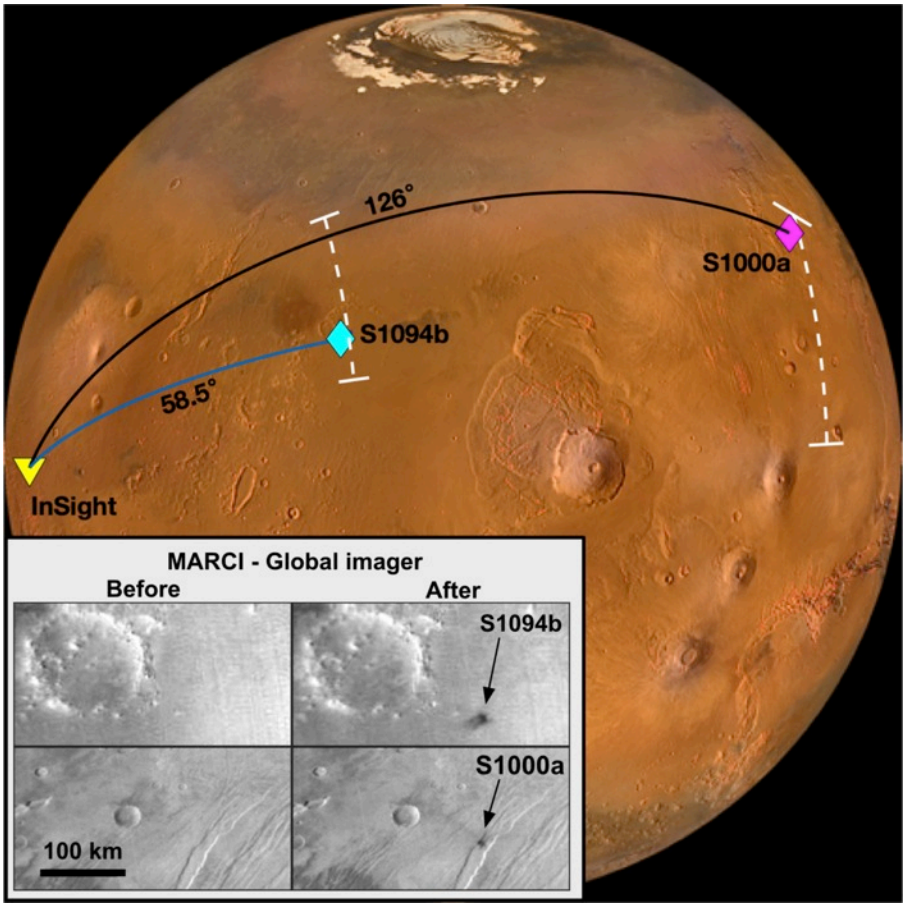

Fig. 1. Impact Event Location Map. The location of the impact craters (diamonds) and the InSight lander (yellow triangle) are shown. The S1094b crater is located at 34.80°N, 189.92°E in Amazonis Planitia. The S1000a crater is located at 38.11°N, 280.12°E in Tempe Terra. The great-circle paths between the new craters and InSight are superimposed onto the underlying globe image derived from MARCI (*13*), Mars Orbiter Camera (*49*) and Mars Orbiter Laser Altimeter data (MOLA) (*50*). The seismic epicentral distance estimates are indicated by the white-dashed lines that extend over the azimuthal uncertainty estimate. The inset shows MARCI images from before and after the impacts. The MARCI images have ~2 km/pixel resolution at nadir.

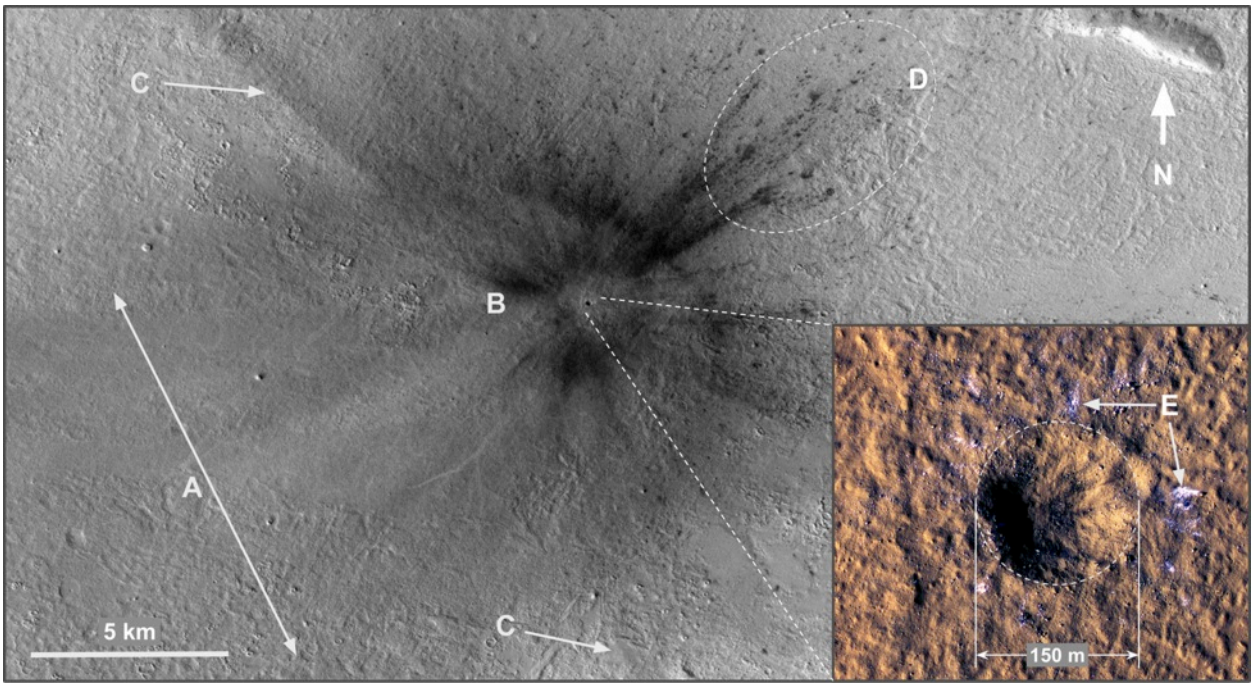

Fig. 2. Orbital images of the impact crater and surrounding area. CTX image (*main panel*): The hypervelocity impactor traveled from SW to NE at an inferred azimuth of ~60^{o} (Fig. S3) creating a Mach cone shockwave that altered the surface albedo up-range of the impact, region A in the figure. The inner dark ring, near B**,** is interpreted to be the result of blast wave mobilization of surface fines, impact derived material directly deposited on the surface, or by ejecta induced disturbances of the surface dust. The absence of up-range ejecta disturbances indicates an oblique (~30^{o} elevation) impact (*15*). Faint arcuate rays, C, emanating cross-track of the impactor were likely caused by the superposition of the Mach cone and the atmospheric blast (*17*) indicating both blast waves propagated out at least 18 km. The long-range ejecta induced disturbances are concentrated in the down-range direction, region D, extending to at least 37 km. HiRISE image (*inset panel*): The crater has a rim-to-rim diameter of approximately 150 meters. The crater floor has an irregular shape with a depth of roughly 21 meters. The light-toned material, e.g., areas indicated by arrows E, around the crater is inferred to be water ice ejected during the impact.
CTX Image ID U05_073077_2154_XI_35N170W. Credit: NASA/JPL-Caltech/MSSS.
HiRISE Image ID ESP_073077_2155. Credit: NASA/JPL-Caltech/University of Arizona

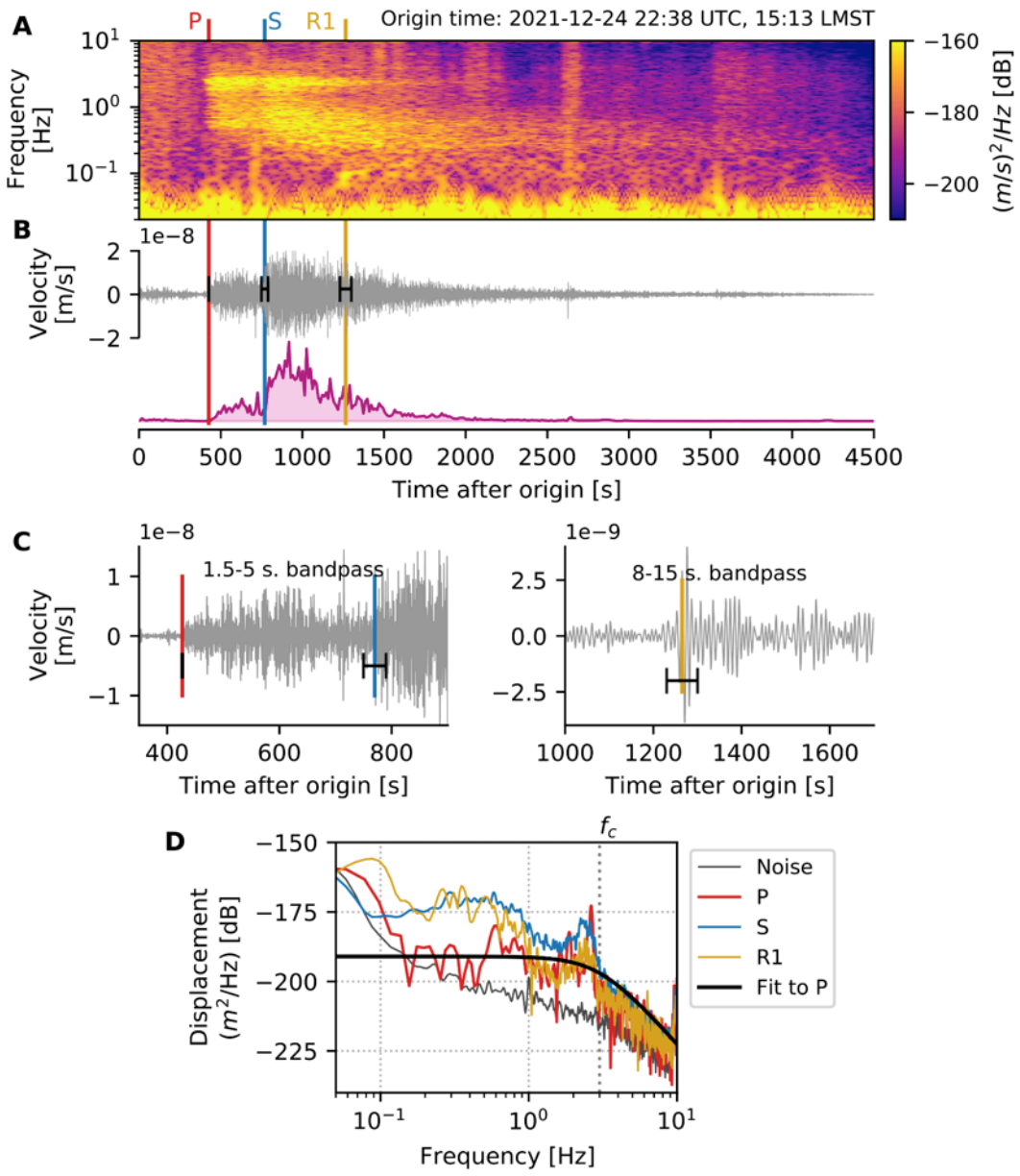

Fig. 3. Seismic observation of S1094b, using de-glitched broadband data. (**A**) Vertical component velocity spectrogram. The event occurs at the end of a noisy period typical of martian afternoons. (**B**) Vertical component velocity time series bandpassed between 1 and 10 sec and derived spectral envelope. Phase picks for P, S, and Rayleigh (R1) wave arrivals are indicated with pick uncertainty indicated by black bars in the timeseries. (**C**) Waveform details of the P and S body waves (left) and Rayleigh wave (right). (**D**) Displacement spectra for the P, S, and Rayleigh waves and pre-event noise. See Fig. S1 for a similar analysis of S1000a.

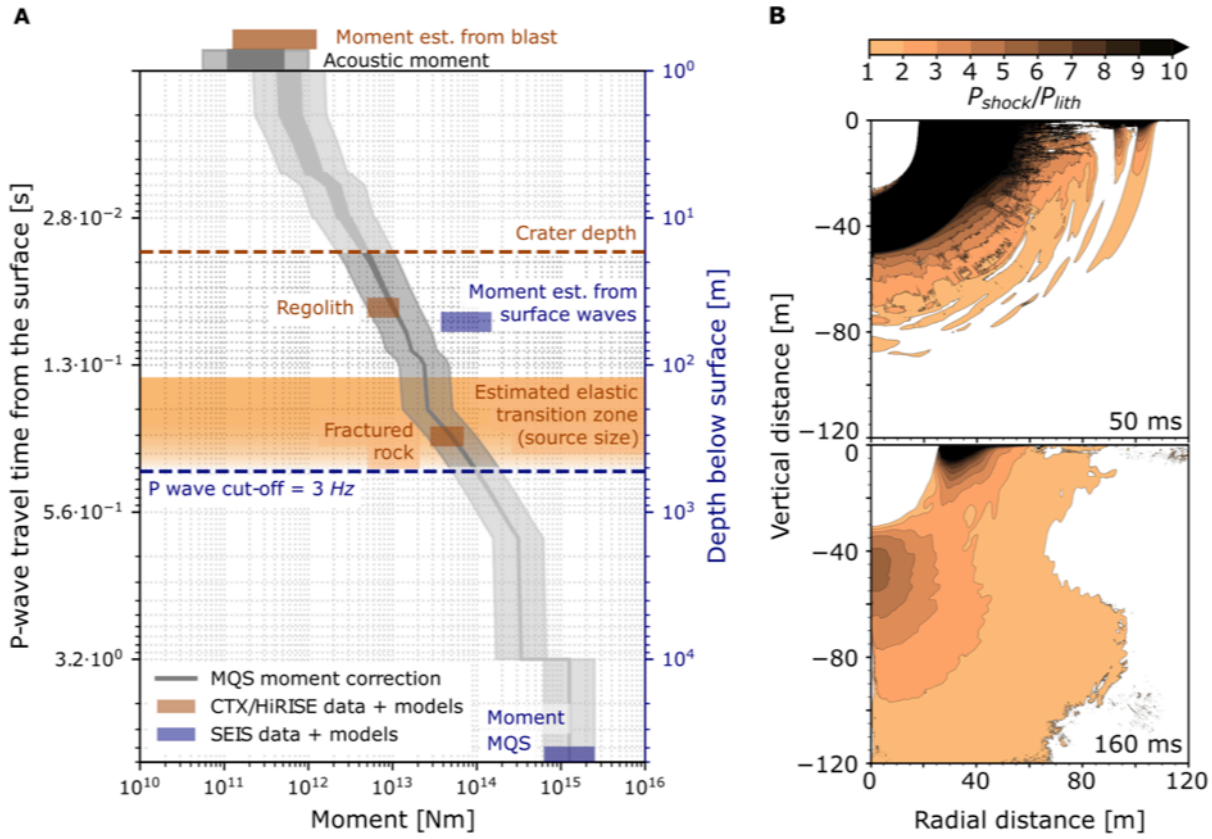

Fig. 4. Seismic source analysis for impact S1094b. (**A**) Seismic moment extrapolated to different source depths and in the air (gray). The blue bars are MQS moment and moment from surface wave amplitude. See more in Fig. S5 and seismic modeling methods Fig. S6. The brown bars show three moment calculations: two seismic moments estimated from crater size assuming different target materials (*29*, *30*) and one acoustic moment at the surface. Note the overlap between the predicted moment from the atmospheric blast and the estimated acoustic moment (brown and gray bars at top of 4A). The orange-shaded region indicates the estimated depth range for the transition from shock to elastic waves (*29*). (**B**) iSALE-2D hydrocode simulation of shock wave caused by a vertical impact at 12 km/s of a 5-m-diameter (180 ton) meteoroid into fractured basalt. Two snapshots at 50 and 160 ms show the zone of seismic wave generation where the shock pressure (P_{shock}) is substantially higher than the lithostatic pressure (P_{lith}).

Science
AAAS

Supplementary Materials for

Largest recent impact craters on Mars: Orbital imaging and surface seismic co-investigation

L. V. Posiolova, P. Lognonné, W. B. Banerdt, J. Clinton, G. S. Collins, T. Kawamura, S. Ceylan, I. Daubar, B. Fernando, M. Froment, D. Giardini, M. C. Malin, K. Miljković, S. C. Stähler, Z. Xu, M. E. Banks, É. Beucler, B. A. Cantor, C. Charalambous, N. Dahmen, P. Davis, M. Drilleau, C. M. Dundas, C. Durán, F. Euchner, R. F. Garcia, M. Golombek, A. Horleston, C. Keegan, A. Khan, D. Kim, C. Larmat, R. Lorenz, L. Margerin, S. Menina, M. Panning, C. Pardo, C. Perrin, W. T. Pike, M. Plasman, A. Rajšić, L. Rolland, E. Rougier, G. Speth, A. Spiga, A. Stott, D. Susko, N. A. Teanby, A. Valeh, A. Werynski, N. Wójcicka, G. Zenhäusern

Correspondence to: posiolov@msss.com

This PDF file includes:

Materials and Methods

Camera descriptions

This study uses three imagers onboard the Mars Reconnaissance Orbiter (MRO) (*51*) that has been orbiting Mars for the past 16 years. The Mars Color Imager (MARCI) is a low-resolution (1–4 km/px), wide-angle camera that acquires daily global maps of the surface and atmosphere (*13*). It is primarily intended for studying the atmosphere, but its daily coverage can provide tight temporal constraints on new large-scale phenomena. The Context Camera (CTX) has a 6deg FOV with a resolution of ~6m/px resulting in an image width of ~30km and up to ~250km along-track (*9*). The High Resolution Imaging Science Experiment (HiRISE) (*18*) has a resolution of 25 cm/px and FOV that results in a 5-km-wide image of the surface.

InSight seismometer description

The InSight mission monitors the seismicity of Mars in order to elucidate the interior structure and formation of the red planet (*11*). In order to achieve this, InSight is equipped with the Seismic Experiment for Interior Structure (SEIS) package (*10*) that includes 2 co-located 3-axis seismometers, the Very Broadband Sensor (VBB) and the Short Period Seismometer (SP), each acquired on a 24-bit digitizer. The VBB was used in this study. InSight landed on Mars on 26 Nov 2018, Sol 0 for the mission. SEIS was placed on the ground on Sol 25, and full protection was achieved on Sol 70 after it was covered by the Wind and Thermal Shield (WTS). In addition to other instrumentation, InSight includes a full weather station (*52*), though due to power constraints, it was not operational at the time of the seismic events discussed. Throughout the mission so far, SEIS operates as expected, achieving and exceeding its target noise levels (*25*).

Imaged Crater and Seismic Impact Characteristics

Table S1. Derived parameters from orbital images and metadata

	S1094b (Amazonis Planitia)	**S1000a (Tempe Terra)**
Latitude (areocentric)	34.8037°N	38.1080°N
Longitude	189.9202°E	280.1229°E
Distance from InSight	3460 km / 58.5°	7460 km / 126.09°
Azimuth from InSight	51.4° (cw rel. North)	34.0° (cw rel. North)
Crater rim diameter	150 m ± 10 m	130 m ± 12 m (largest)
Crater rim-to-floor depth	21 m ± 3 m	17 m ± 5 m
Impactor bearing	60° ± 5° (cw rel. North)	130° ± 15° (cw rel. North)
MARCI pre-impact image	U03_072246_1470_MA_00N157W 2021-12-24 18:10:12 UTC	N22_070990_1006_MA_00N063W 2021-09-17 21:18:27 UTC
MARCI post-impact image	U03_072259_1475_MA_00N152W 2021-12-25 18:29:23 UTC	N22_071004_1011_MA_00N086W 2021-09-18 23:29:01 UTC
CTX pre-impact image	K18_060561_2175_XI_37N170W 2019-06-28	K09_056852_2181_XN_38N079W 2018-09-12
CTX post-impact image	U05_072866_2134_XN_33N169W	U06_073311_2186_XI_38N079W

	2022-02-11	2022-03-17
HiRISE image	ESP_073077_2155 2022-02-27	ESP_073522_2185 2022-04-03

Table S2. Impact event characteristics from SEIS/MQS

	S1094b	**S1000a**
Latitude	44.32°N	23.59°N
Longitude	173.54°E	271.07° E
Distance from InSIght	3530 km ± 360 km 59.6°±6.1°	7592 ± 1220km (using SS and PP) 128.3°±19°
Azimuth from InSight	40° (range 31°-58°)	55° (range 29.3°-70.3°) (*53*)
Distance and azimuth probability distributions	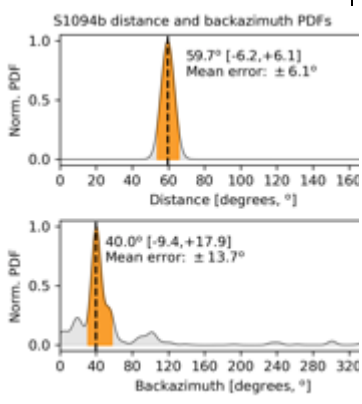	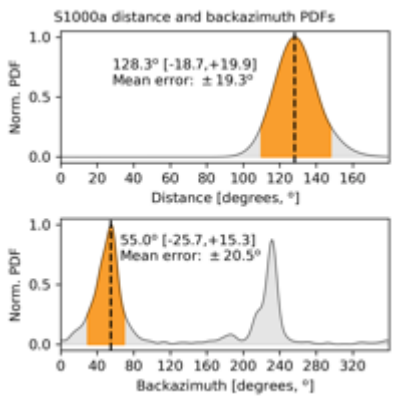
Origin Time (at the source)	2021-12-24 22:38:02±23s UTC (~18:49 LMST Ls=147)	2021-09-18 17:46:20 ±62 UTC (~10:23 LMST Ls=101)
Duration	107.53 min	94.11 min
P (or PP) arrival time (at InSight)	2021-12-24 22:45:09 ± 1s UTC (~15:20 LMST)	2021-09-18 18:01:47± 20s UTC (~01:02 LMST)
S (or SS) arrival time	2021-12-24 22:50:52 ± 20s UTC	2021-09-18 18:14:08 ± 60s UTC
Amplitude of the P (or PP)	1.39×10^{-9} m	1.30×10^{-9} m

Amplitude of the S (or SS)	4.64×10^{-9} m	3.22×10^{-9} m
Moment Magnitude	4.0 ± 0.2	4.1 ± 0.2
Corner frequency	3 Hz	1.5 Hz
Moment	1.26×10^{15} Nm (6.3×10^{14}-2.5×10^{15} Nm)	1.78×10^{15} Nm (8.9×10^{14}-3.5×10^{15} Nm)
Location error map	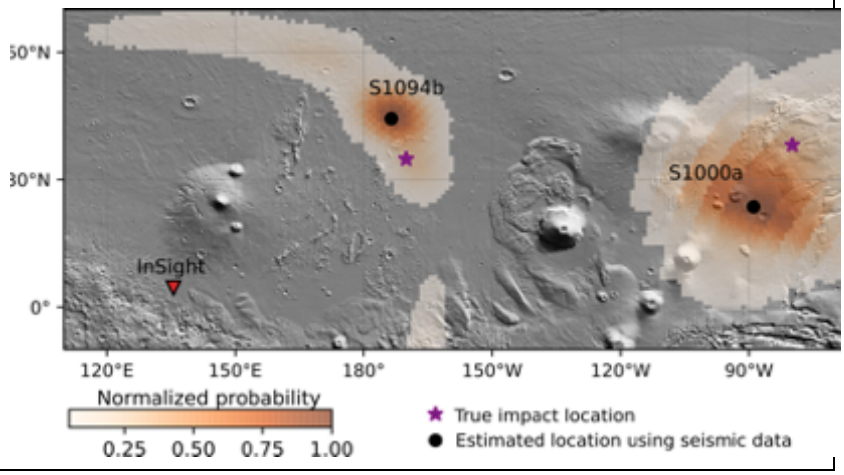	

Table S2 is a summary of the seismic characteristics of the two impacts: S1094b (left column) and S1000a (right column). Information is from MQS (*41*, *43*). The distance and back azimuth probability density functions (PDF) for each event with error estimates are also provided. For the uncertainty estimates, we first normalize the individual PDFs by their maximum. Then we fit a univariate spline to these discrete PDFs to account for the distribution skewness. Finally, the error bounds (orange shaded regions) are calculated from the zero-crossings at a baseline of 75% from the maxima, assuming these values represent the 2-σ uncertainties. The indicated mean errors are the arithmetic means of the bounds in square brackets. The final location error is shown on a map view, where combined probabilities below 0.05 are masked for visual clarity.

Seismic Analysis of Event S1000a

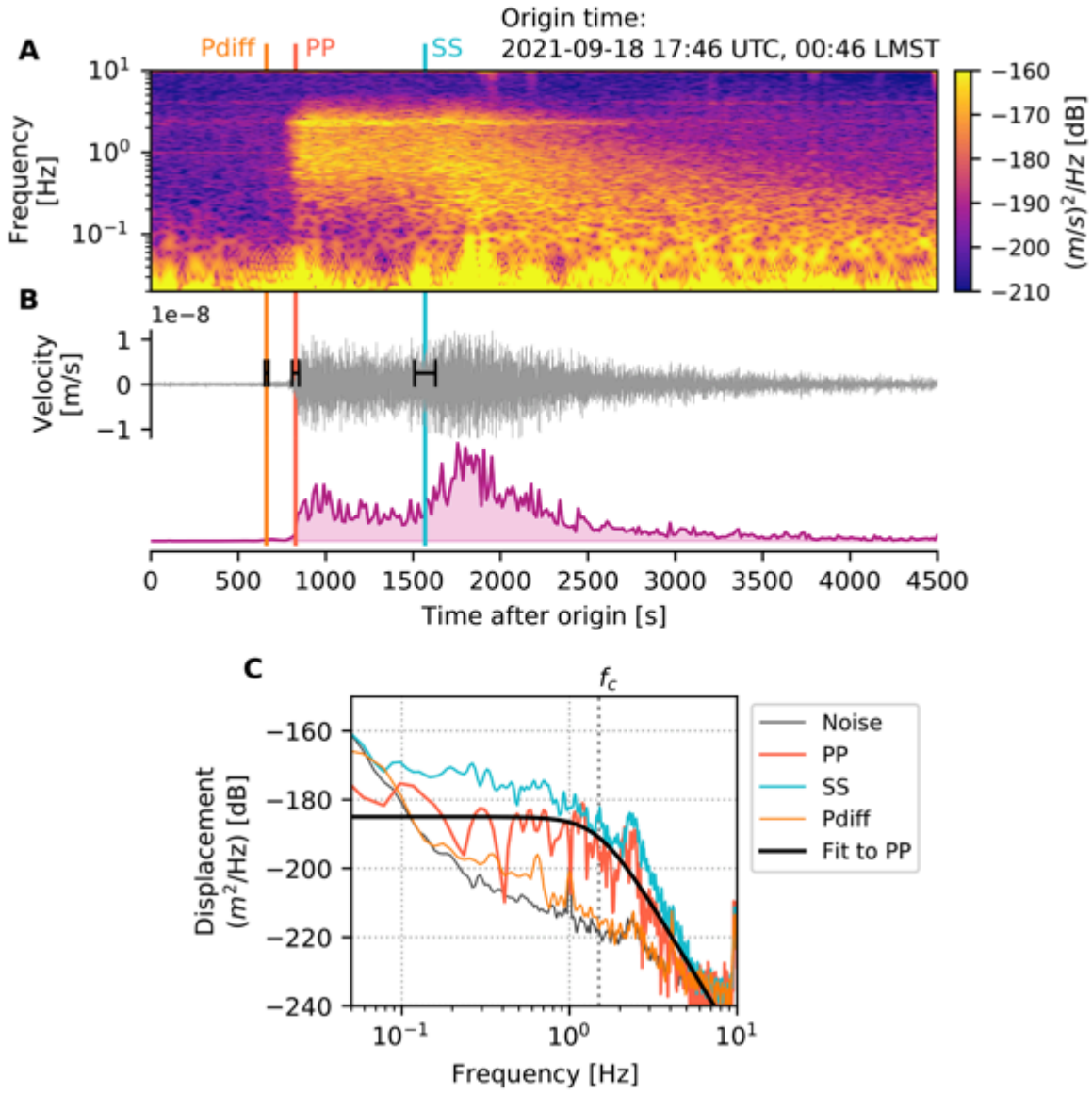

Fig. S1. Seismic observation of S1000a. The graphs are made using de-glitched VBB data. (**A**) Vertical component velocity spectrogram. The event occured during a seismically quiet period (early morning at InSight). (**B**) Vertical component velocity time series bandpassed between 1 and 10 s and derived spectral envelope. Phase picks for P_{diff}, P- and S-wave arrivals are indicated, with pick uncertainty indicated by black bars in the timeseries. (**C**) Displacement spectra for short time windows shortly after the PP- and SS-arrivals and the pre-event noise. The PP spectral fit is made with a corner frequency of 1.5 Hz with a decay proportional to f^{-4}, high-frequency roll-off. This slope likely exceeds the source roll off, but accounts for effects of attenuation which has therefore erased the source information. The long-period plateau from which the magnitude is computed is at A0=-185dB (*28*). See (*14*) for a detailed discussion of the phase picks and other seismic aspects of this event.

Impact Site Imagery for S1000a

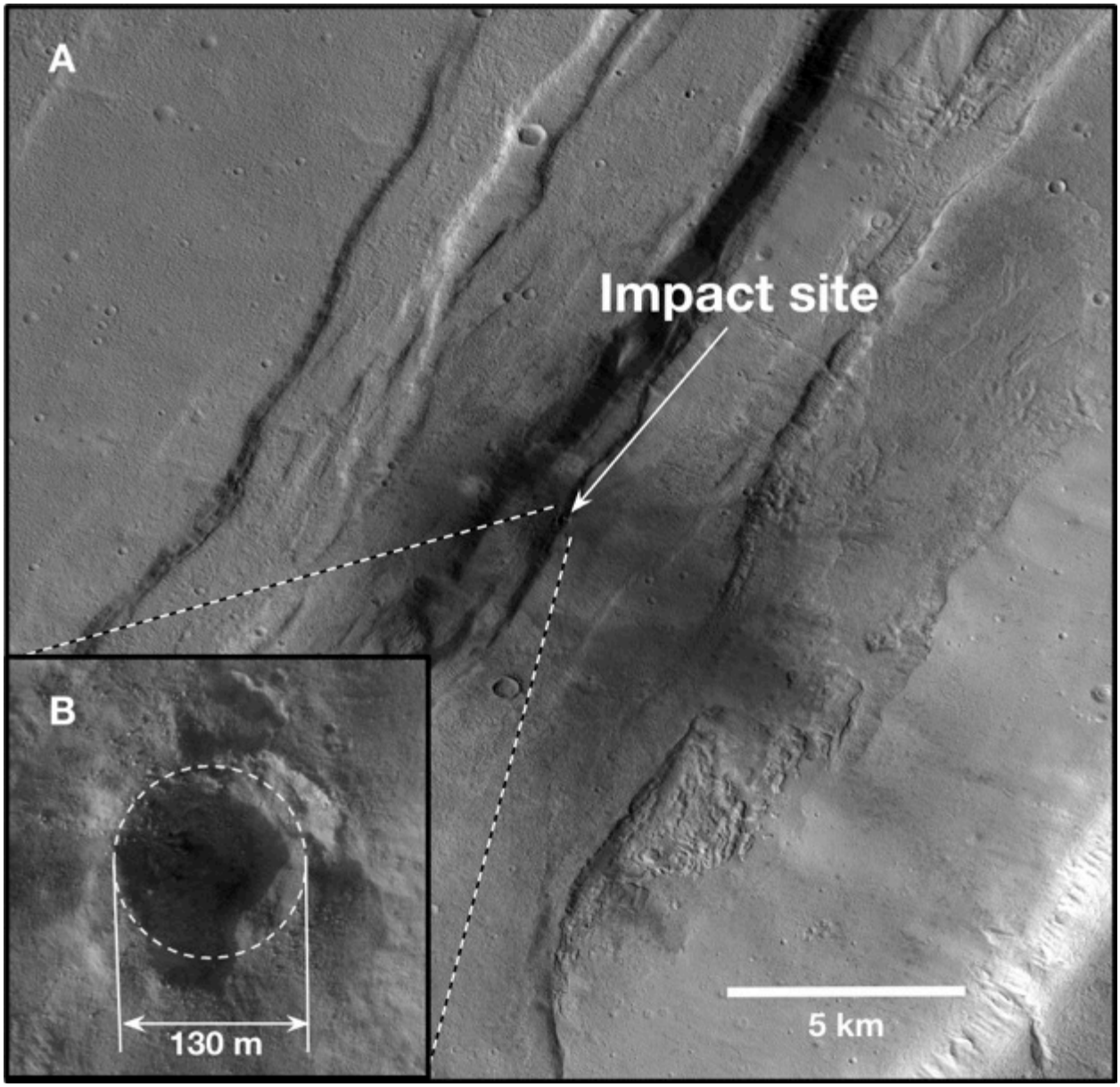

Fig. S2. Imagery of crater associated to S1000a. (**A**) The CTX image shows the impact crater and surrounding blast zone that is associated with seismic event S1000a. It occurred in the Tempe Terra region of Mars. The site has considerably more topographic relief compared to the Amazonias impact S1094b. The impactor struck a graben wall that disrupted the blast zone, and the albedo variations are more diffuse than seen for S1094b. (**B**) The HiRISE image reveals that the impact site consists of multiple craters with the largest (white dash circle) having an estimated diameter of 130±12 meters.
CTX Image Credit: NASA/JPL-Caltech/MSSS
HiRISE Image Credit: NASA/JPL-Caltech/University of Arizona

Analysis of Blast Zone Surrounding S1094b Impact Site

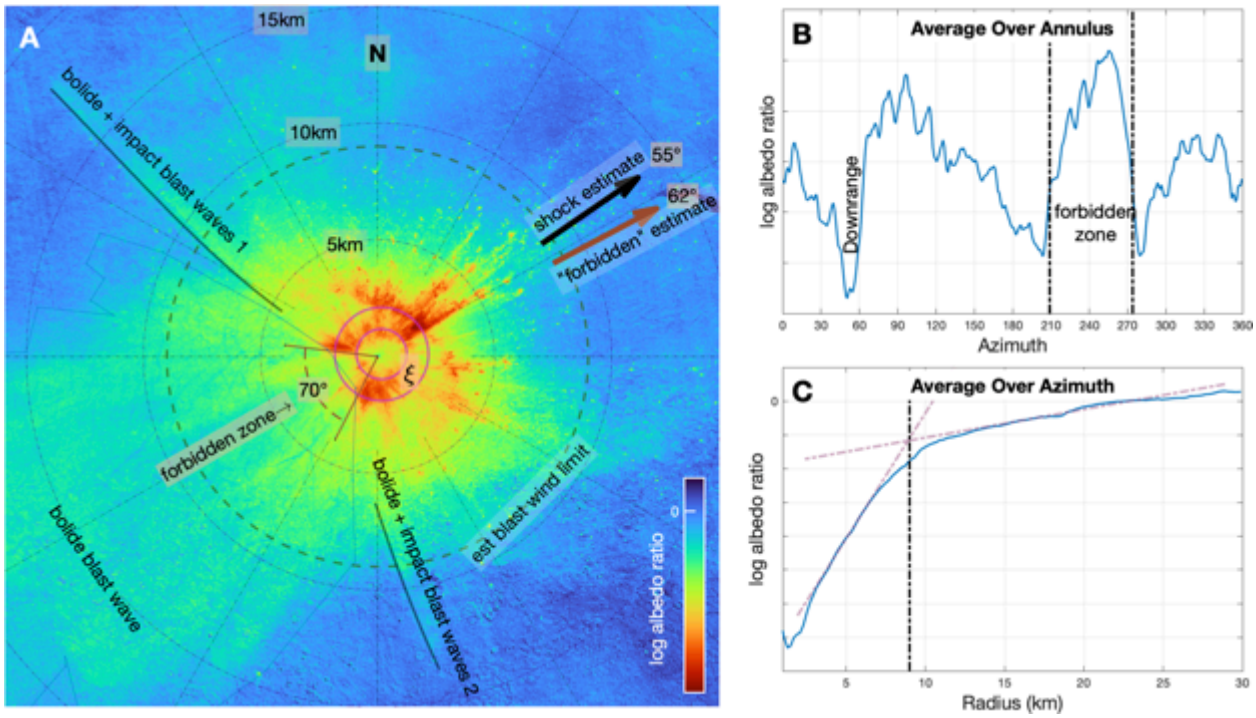

Fig. S3. Albedo residual between before and after images for S1094b. (**A**) Color map showing the log ratio between before and after impact CTX images. Images were map projected and scaled to minimize the RMS of the log ratio away from the blast zone; the color map shows relative variations in albedo between images. The log ratio tends to zero (log(1)) at far distances, as expected. In the residual image, the extent of the albedo disturbance from the bolide blast wave is evident to the southwest. The two, slightly arcuate rays ("scimitars" labeled 'bolide+blast waves 1 and 2') are visible with the northwestern ray extending to at least 18 km. These are believed to follow the intersection of the conical blast wave from the hypervelocity bolide and the hemispherical atmospheric blast created upon impact (*17*). Because the two blast waves are likely symmetrical, the angle between the rays can be used to estimate the impactor's direction of travel (55^o). The ring of dark linear rays (red) surrounding the crater displays a classic asymmetrical pattern associated with oblique impactors (*15*). This provides another method to estimate the direction of travel. To estimate the extent of the "forbidden zone" in a systematic manner, we average the residual albedo across the annulus (labeled $\boldsymbol{\xi}$) that contains the highest concentration of dark linear rays. (**B**) The radial averaged log ratio albedo residual over annulus $\boldsymbol{\xi}$ versus azimuth. The edges of the "forbidden zone" are chosen at the steepest slopes in the residual plot. This results in a 70^o arc for the forbidden zone (at 1–2 km radius). Bisecting the angle results in a trajectory estimate of 62^o clockwise from north. This is in rough agreement with the scimitar ray estimate. The travel direction is further confirmed by the concentration of rays in the downrange direction as expected for an oblique impact between 55^o and 60^o from north. (**C**) The azimuthal averaged log ratio albedo residual versus radial distance from the central crater. In order to estimate the size of the atmospheric blast, a measure of the blast zone that can be related to blast energy is needed. Semi-empirical airblast theory (*35*) extrapolated to Mars — a relation between radial wind speed and blast size (Fig. S4). Combining this

relation with approximate minimum thresholds for the removal of surface dust provides a mechanism for determining the rough size of the blast. We examine the albedo residual map to estimate the limit of dust disturbance by the impact blast. In order to make this less subjective, we average the albedo residual over azimuth and examine the ratio versus radial distance. A break in the slope at 9 km makes for a reasonable estimate for the dust disturbance limit. This is consistent with the predicted limits in Fig. S4.

(CTX image IDs: G18_025234_2165_XN_36N170W & U05_073077_2154_XI_35N170W).

Determining Atmospheric Blast Energy

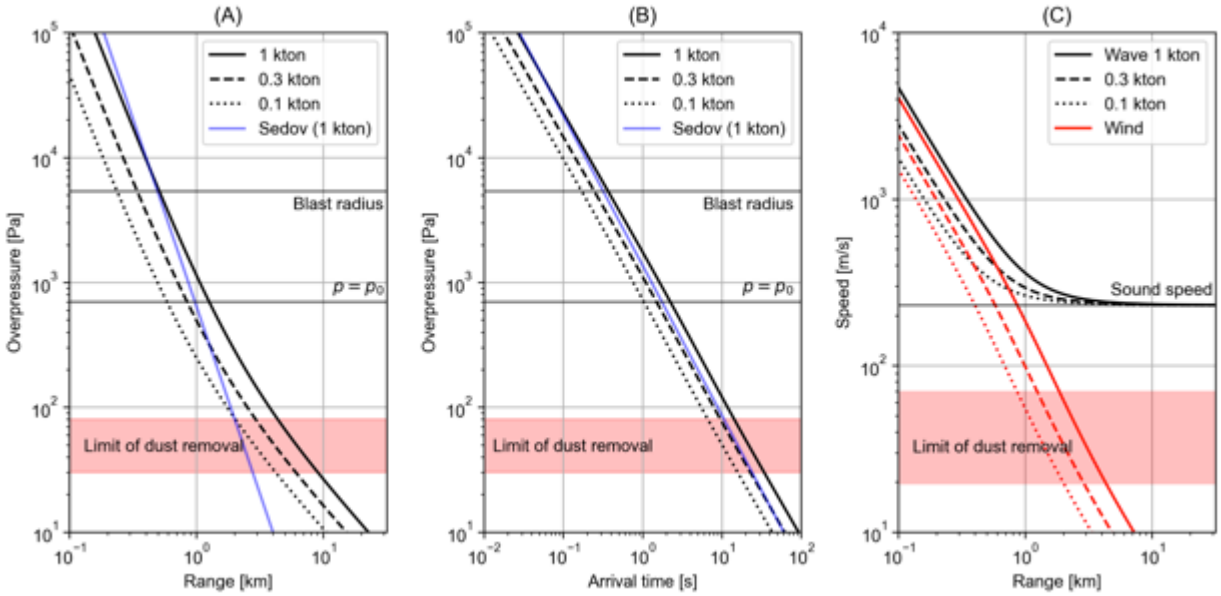

Fig. S4. Atmospheric blast wave models. Each panel includes estimated values for three different blast energies (1 kton TNT equivalent, 4.184×10^{12} J; 0.3 kton and 0.1 kton), based on nuclear explosion tests (*35*) scaled to Mars atmospheric conditions (ratio of specific heats = 1.3, surface density = 1.7×10^{-5} kg m^{-3}, reference sound speed = 230 m/s, surface pressure 700 Pa). Overpressure as a function of (**A**) distance and (**B**) arrival time. (**C**) Blast wave speed (black) and maximum wind speed behind the blast (red) as a function of distance. Also included in (A) and (B) is the case for a spherical 1-kton blast in the strong shock regime (*54*), inside the blast radius. Approximate minimum thresholds for removal of surface dust are shown for pressure (30–80 Pa) (*55*) and wind speed (20–70 m/s) (*56*).

Methodology for moment correction

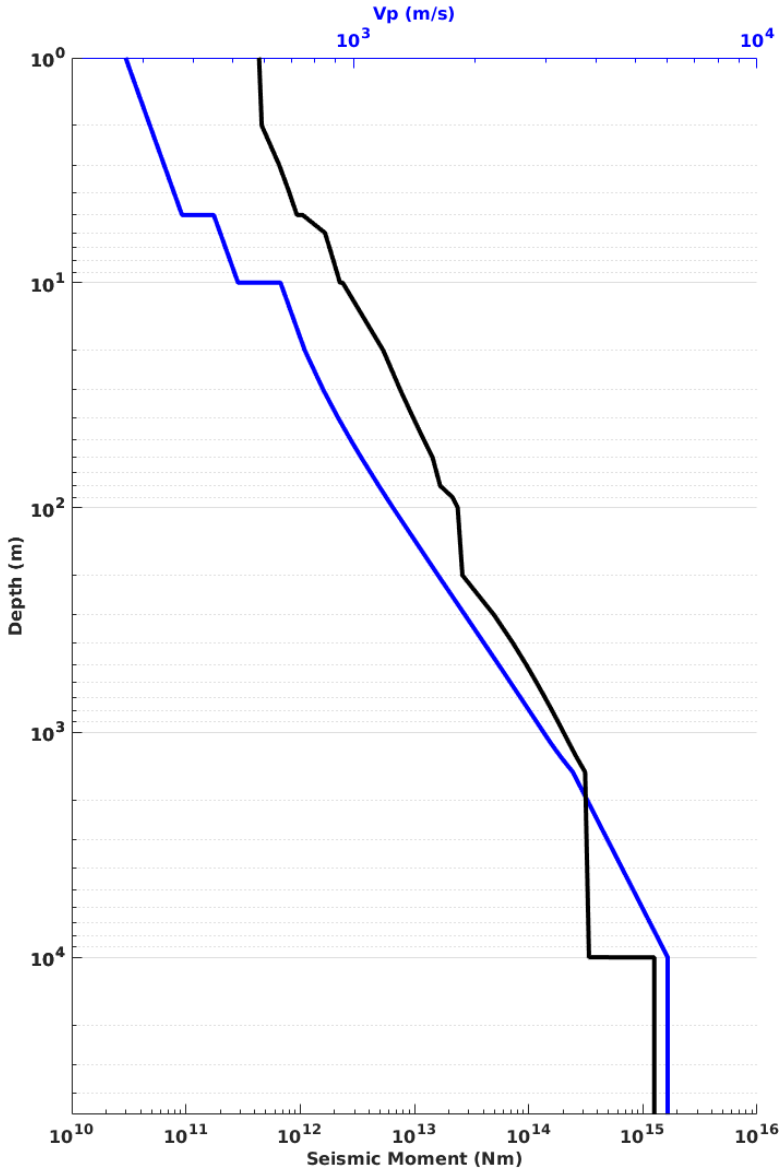

Fig. S5. The S1094b seismic moment (black) and the P-wave velocity model (blue). The MQS seismic moment estimate at 50 km depth is calculated based on the P-wave amplitude and the assumption that the seismic source is in a crustal medium with V_P=6000 m/s and V_S=3500 m/s (*42*). However, the S1094b source is at shallow depth thus we need to correct the MQS moment estimate. Since P-wave amplitude depends on the medium around the source (*57*), we need a velocity model (blue) for the correction. We adopt a lava-flow velocity model (*58*) with the crustal medium as the half-space starting at 10 km depth (*59*). To achieve the correct seismic moment for a source above the half-space, we calculate the P-wave amplitude (A) in the half-space from the source as

$$A = \frac{M_S}{\rho_s \alpha_s^3} T = \frac{M_C}{\rho_c \alpha_c^3}$$

where M_s is the seismic moment at the source depth; $\boldsymbol{\rho}_s$ and $\boldsymbol{\alpha}_s$ are the density and P-wave velocity of the medium around the source, respectively. T is the P-wave transmission coefficient from the source to the half-space (*57*) and we use a vertically down-going P wave. The second equality sign means that the amplitude from the shallow source is equal to that from the source at depth given by the MQS moment, M_c. $\boldsymbol{\rho}_c$ and $\boldsymbol{\alpha}_c$ are the density and P-wave velocity in the crustal half-space, respectively. Thus, the source moment is written as

$$M_S = \frac{\rho_s \alpha_s^3}{\rho_c \alpha_c^3 T} M_c$$

We apply the above equation to each depth above the half-space (black). For the seismic source in the Martian atmosphere (i.e., the impact airblast), we expand the above calculation to the air density (0.015 kg/m^3) and acoustic-wave velocity (220 m/s) to calculate the corresponding acoustic moment in the atmosphere. These acoustic or seismic moments in the air or at each depth can generate the same P-wave amplitude in the crustal half-space as the MQS moment (Fig. 4A).

Modeling Crater Formation

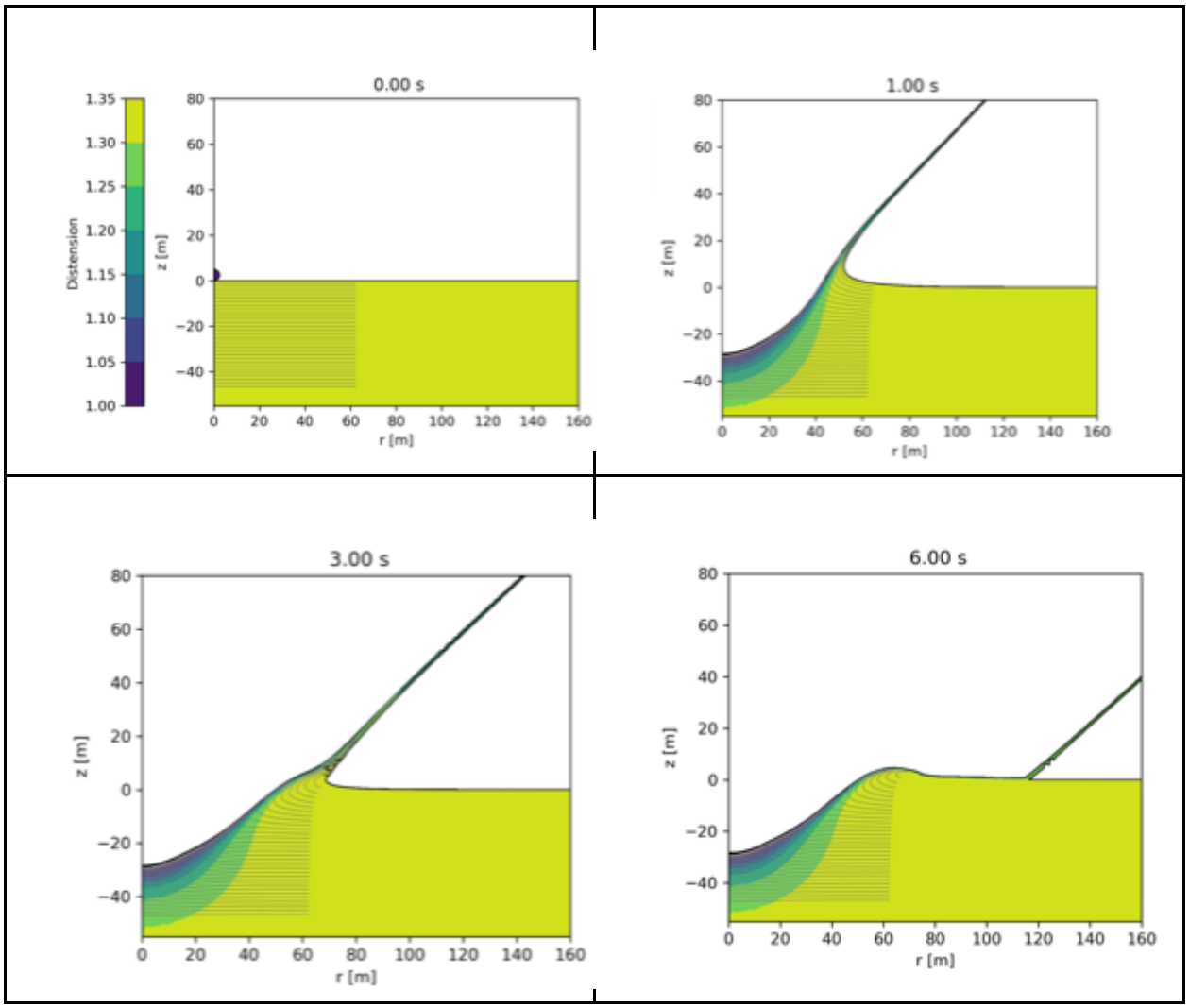

Fig. S6. Time series of the crater formation. Calculations are from the iSALE-2D shock physics code (*60–62*), ranging from top left to bottom right. Cylindrical symmetry is applied around the vertical axis; r denotes the radial distance from the impact point and z distance above and below the surface level (depth). Lines indicate local stratigraphy. Distension denotes the change in the target porosity, starting with 25%. Distension is equivalent to 1/(1-porosity). The crater floor experienced a decrease in porosity due to compaction and compression during the crater excavation phase. The final crater is comparable to the observed crater dimensions, the rim-to-rim diameter being 130 m and final depth 28 m. Excavation depth is up to 10 m made within 2.5 seconds. The final crater formed within 8 seconds. This iSALE-2D simulation was made using a 5-m diameter basalt projectile at 12 km/s vertical impact speed. The target was assumed to be fractured bedrock used in previous works (*63*). Considering that the observed crater is irregular in morphology, and likely made under an oblique impact incidence into a heterogeneous medium, the simulated crater represents a simplified model that connects estimated impact conditions with the expected

crater size. It is possible that some post-impact slumping could cause the reduction of crater depth and slightly extend crater diameter.

Surface wave seismic moment analysis

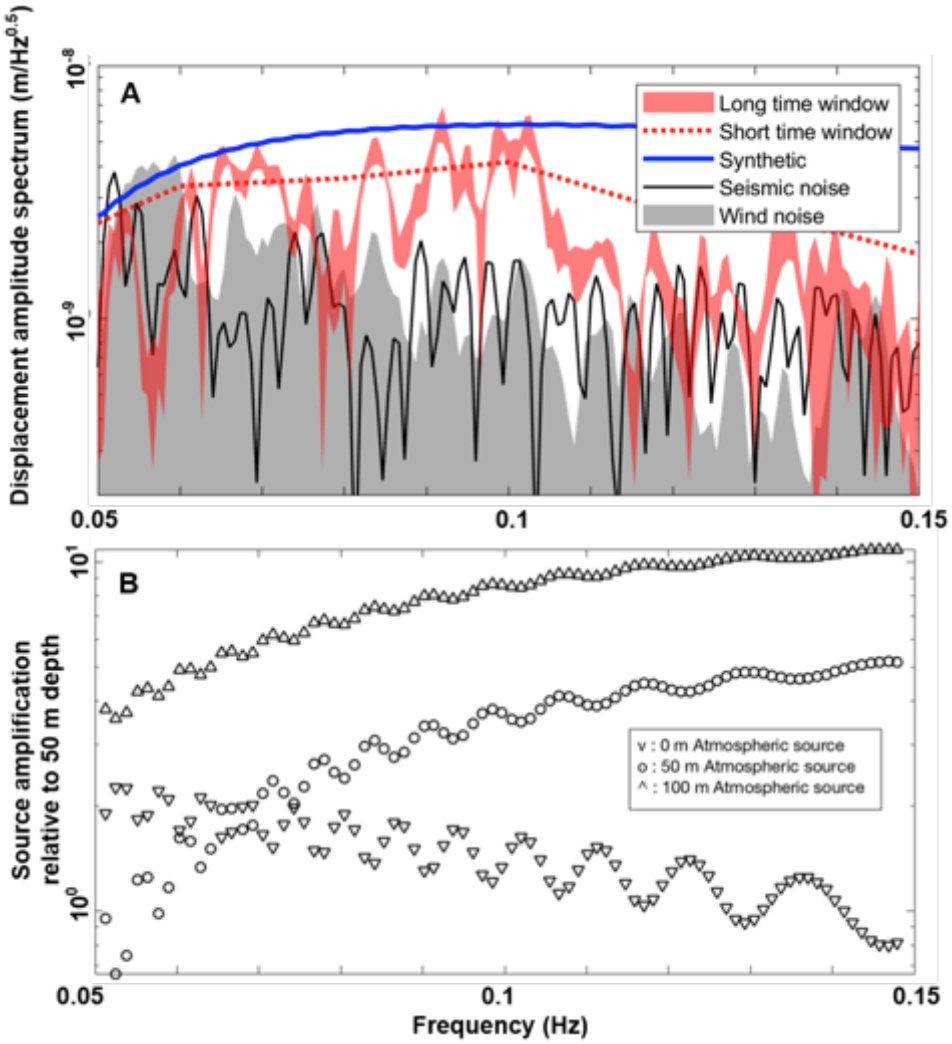

Fig. S7. Surface wave seismic moment estimation. (**A**) Seismic moment estimation of S1094b surface wave spectral amplitude and (**B**) the surface-wave amplification ratios of atmospheric sources relative to a 50-m-depth source. We measure the S1094b surface-wave vertical-component spectra from three time windows (300/400/500-s-long) starting at 1,150 s after the event origin. Maximum and minimum of the three spectra at each frequency are shown in red. We use these long time windows for high spectral resolution. To check the effect of a short time window, we use 40-s-long time windows from 1,150s to 1,650s after the origin time with 10% overlap between two adjacent time windows; the mean value of these spectra is plotted in a red dotted line. The seismic noise is computed from three time windows (300/400/500-s-long) ending at 1,150 s, and we plot the maxima in black. We compute wind noise in the vertical component by assuming the long-period horizontal component is due to wind. Thus, we estimate the wind noise (gray) using the compliance theory (*64*) and a 2-m/s environmental wind speed. The wind speed is from fitting the elliptical part of the vertical- and horizontal-component data before 1,150 s. The synthetic surface-wave spectral amplitude (blue) is obtained from normal mode summation (*65*), where normal modes are computed for the lava-flow model (*58*) with a source at 50 m depth. The

seismic moment is 7.5×10^{13} Nm. Note that this seismic moment is a lower bound for the Rayleigh wave, as the 3D scattering effects will further reduce the amplitude. (B) The amplification ratios are the normal-mode amplitude ratios between the 50-m-depth source and three atmospheric sources at different altitudes. The normal modes for the atmospheric sources are computed with the Mars atmosphere model (*66*, *67*) following (*39*), integrating both a radiating boundary condition at the top of the atmosphere and viscosity and relaxation of the CO2 atmosphere. See more details on such normal-mode computation for Mars in (*39*) and (*32*). Amplification with source altitude is largely dependent on the upward acoustic propagation of the Rayleigh wave which depends on $\Re\left[i \cdot e^{\,i2\pi fz/c}\right]$ for excitation coefficients (*68*, *69*), where c is the acoustic sound speed, z is the altitude, and f is the frequency. This amplification is not observed in the S1094b SW spectrum between 0.1 Hz and 0.15 Hz. Instead, the amplitude roughly decays proportional to f^{-2}. The shape of the surface wave spectra, including amplitude modulation features, is closer to the source located near the surface as compared to below the surface or substantially above the surface. This observation suggests a larger seismic moment release near the surface.

Estimating Impactor Momentum

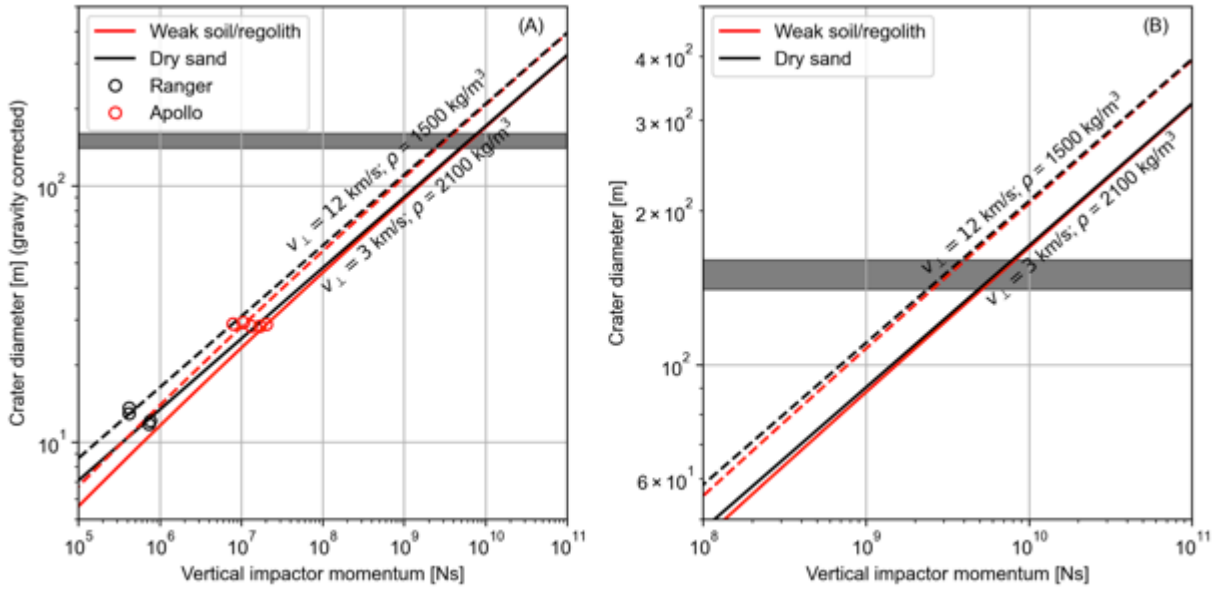

Fig. S8. The relationship between impactor momentum and crater diameter. (**A**) The panel shows crater diameter as a function of the vertical component of impactor momentum for impacts on Mars in porous, weak granular target materials. (**B**) Enlarged version of (A) showing more detail for the crater sizes found in this study. Craters formed by artificial impacts on the Moon (*68*) are shown for comparison (circles), with diameters corrected for the difference in surface gravity between the Moon and Mars. Crater-scaling relationships (*69*) are shown for two possible target types: dry cohesionless sand (black) and a weakly cohesive porous soil or regolith (red); and two combinations of vertical impact speed and target density. The effect of target cohesion is minimal at the size of the newly discovered crater (gray shading). The estimated range of vertical impactor momentum is 2–8 × 10^9 Ns.

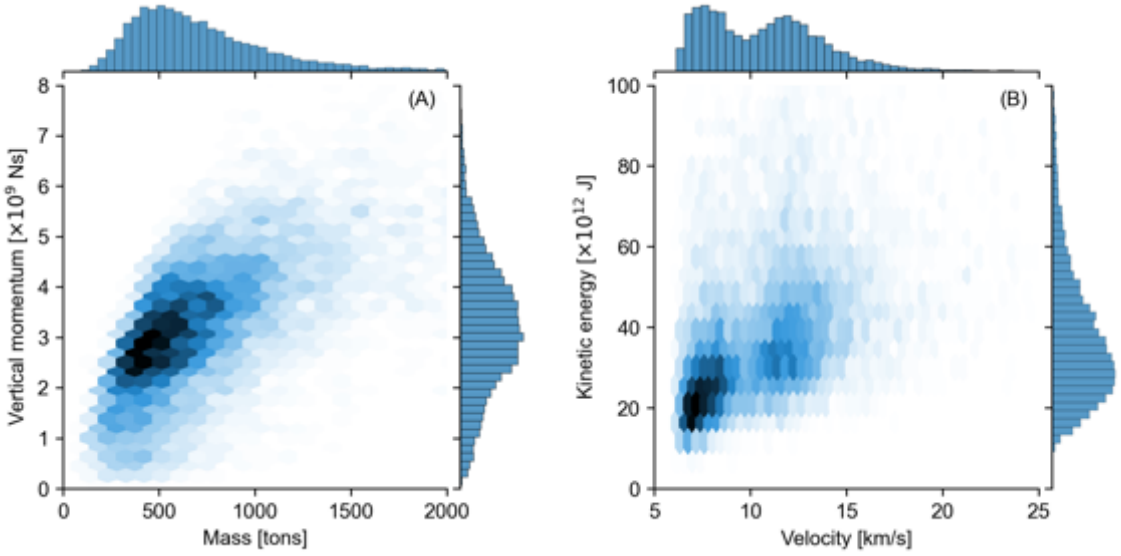

Fig. S9. Statistical analysis of impactor parameters. Vertical impactor momentum versus impactor mass (**A**) and impactor kinetic energy versus impact velocity (**B**) that produce a 150-m-diameter crater on Mars. Results are shown for 10,000 impact scenarios according to the scaling relationship for weak soil shown in Fig. S8 after atmospheric entry. Scenarios are sampled from prior frequency distributions for impact velocity based on the estimated velocity frequency distribution for Mars (*70*); impactor mass based on the mass frequency distribution of terrestrial fireballs (*71*); impact angle based on an isotropic impact flux (*72*) and a uniform impactor density frequency distribution with range 1400–4000 kg/m^3. Fragmentation of the meteoroid is neglected. For the range of likely impact scenarios, the effect of atmospheric deceleration is negligible.

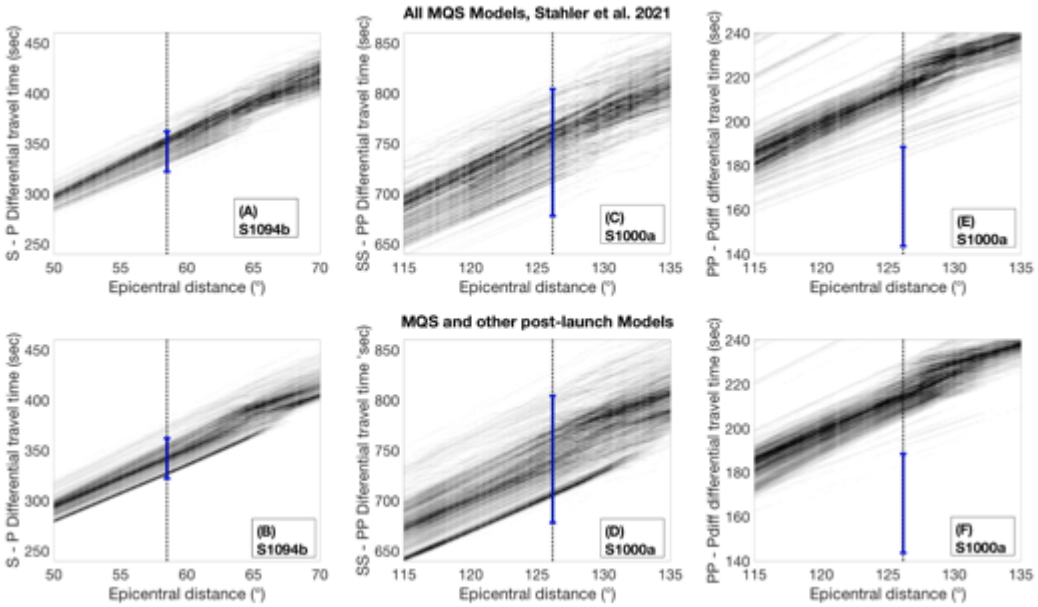

Fig S10. Comparison of observed and modeled differential travel times.

The observed differential travel times are shown as the blue error bars placed at the crater-to-InSight distance (dashed vertical line). Panels (**A**) and (**B**) show S1094b S-P times, panels (**C**) and (**D**) show S1000a SS-PP times, and panels (**E**) and (**F**) show S1000a PP-P_{diff} times. Predicted differential travel times were calculated using the "Tau-p toolkit" (*73*). The top row shows results for 300 models (*45*) used by MQS for estimating seismic locations (for a source at the surface). The bottom row includes three additional post-launch families of models (*44*, *46–48*). This illustrates the calibration capability of the two impacts for improving velocity models corresponding to the P, S, PP, SS paths, sensitive down to about 800 km.

The S1000a P_{diff} phase is the first seismic wave we have detected on Mars that is sensitive to P-velocities between 800 km and the CMB (*14*). Current models estimate P-velocities below 800 km by using S-velocity models that were constrained based on ScS seismic waves and V_P/V_S ratios estimated from mineralogical and geodynamical models, e.g. (*44*, *46–48*).

We note a significant offset of at least 20 seconds between observations and models. A portion of the time residual (5-10 sec) could be related to the larger crustal thickness at the epicenter and the PP reflection point compared to the crustal thickness predicted at InSight and Cerberus Fossae (*74*). The remaining time residual is a key datum to constrain P-velocity models below 800 km.